

The JWST/AURORA Survey: Multiple Balmer and Paschen Emission Lines for Individual Star-forming Galaxies at $z = 1.5 - 4.4$. I. A Diversity of Nebular Attenuation Curves and Evidence for Non-Unity Dust Covering Fractions

NAVEEN A. REDDY,¹ ALICE E. SHAPLEY,² RYAN L. SANDERS,³ MICHAEL W. TOPPING,⁴ RICHARD S. ELLIS,⁵ MAX PETTINI,⁶ GABRIEL BRAMMER,^{7,8} FERGUS CULLEN,⁹ NATASCHA M. FÖRSTER SCHREIBER,¹⁰ ALI A. KHOSTOVAN,³ DEREK J. MCLEOD,⁹ ROSS J. MCLURE,⁹ DESIKA NARAYANAN,^{11,12} PASCAL A. OESCH,^{13,7,8} ANTHONY J. PAHL,¹⁴ CHARLES C. STEIDEL,¹⁵ AND DANIELLE A. BERG¹⁶

¹*Department of Physics and Astronomy, University of California, Riverside, 900 University Avenue, Riverside, CA 92521, USA; naveenr@ucr.edu*

²*Department of Physics & Astronomy, University of California, Los Angeles, 430 Portola Plaza, Los Angeles, CA 90095, USA*

³*Department of Physics and Astronomy, University of Kentucky, 505 Rose Street, Lexington, KY 40506, USA*

⁴*Steward Observatory, University of Arizona, 933 North Cherry Avenue, Tucson, AZ 85721, USA*

⁵*Department of Physics & Astronomy, University College London, Gower St., London WC1E 6BT, UK*

⁶*Institute of Astronomy, Madingley Road, Cambridge CB3 0HA, UK*

⁷*Niels Bohr Institute, University of Copenhagen, Lyngbyvej 2, DK2100 Copenhagen, Denmark*

⁸*Cosmic Dawn Center (DAWN), Copenhagen, Denmark*

⁹*Institute for Astronomy, University of Edinburgh, Royal Observatory, Edinburgh EH9 3HJ, UK*

¹⁰*Max-Planck-Institut für extraterrestrische Physik (MPE), Giessenbachstr. 1, D-85748 Garching, Germany*

¹¹*Department of Astronomy, University of Florida, 211 Bryant Space Sciences Center, Gainesville, FL 32611 USA*

¹²*Cosmic Dawn Center at the Niels Bohr Institute, University of Copenhagen and DTU-Space, Technical University of Denmark*

¹³*Department of Astronomy, University of Geneva, Chemin Pegasi 51, 1290 Versoix, Switzerland*

¹⁴*The Observatories of the Carnegie Institution for Science, 813 Santa Barbara Street, Pasadena, CA 91101, USA*

¹⁵*Cahill Center for Astronomy and Astrophysics, California Institute of Technology, MS 249-17, Pasadena, CA 91125, USA*

¹⁶*Department of Astronomy, The University of Texas at Austin, 2515 Speedway, Stop C1400, Austin, TX 78712, USA*

ABSTRACT

We present the nebular attenuation curves and dust covering fractions for 24 $z = 1.5 - 4.4$ star-forming galaxies using multiple Balmer and Paschen lines from the JWST/AURORA survey. Nebular reddening derived from Paschen lines exceeds that from Balmer lines for at least half the galaxies in the sample when assuming the commonly-adopted Galactic extinction curve, implying the presence of optically-thick star formation. The nebular attenuation curves exhibit a broad range of normalizations ($R_V \simeq 3.2 - 16.4$). Motivated by the offsets in reddening deduced from the Balmer and Paschen lines, and the high R_V values for the individual nebular attenuation curves, both of which suggest variations in the dust-stars geometry, we propose a model with a subunity dust covering fraction (f_{cov}). Fitting such a model to the H I recombination line ratios indicates $f_{\text{cov}} \sim 0.6 - 1.0$. The normalizations of the nebular attenuation curves, R_V , are driven primarily by f_{cov} and the mix of optically-thick and thin OB associations. Thus, the diversity of nebular attenuation curves can be accommodated by assuming dust grain properties similar to that of Milky Way sightlines but with a subunity covering fraction of dust. Integrated measurements of multiple Balmer and Paschen lines can be used to place novel constraints on the dust covering fraction towards OB associations. These, in turn, provide new avenues for exploring the role of dust and gas covering fraction in a number of relevant aspects of high-redshift galaxies, including the impact of stellar feedback on ISM porosity and the escape of Ly α and Lyman continuum radiation.

Keywords: ISM: dust, extinction — galaxies: evolution — galaxies: high-redshift — galaxies: ISM — galaxies: star formation

1. INTRODUCTION

The accessibility of rest-frame optical and near-infrared recombination and collisionally-excited emission lines afforded by recent advances in ground-based near-IR instruments and space-based missions has motivated detailed modeling of the ISM in distant star-forming galaxies. These advances, when combined with ISM studies of nearby star-

forming regions and galaxies, have enabled evolutionary studies of the state of the ISM throughout most of cosmic history. Among the most critical of the commonly observed rest-frame optical and near-infrared emission lines from the ISM are the Balmer and Paschen series recombination lines of hydrogen. These lines, in concert with those from other ionic species, are used to constrain the chemical abundances, gas densities, temperatures, and the ionization structure of

the ISM. The hydrogen recombination line ratios constitute an ideal probe of the dust column density towards H II regions owing to the cosmic abundance of hydrogen and the insensitivity of these ratios to gas density and temperature over the ranges typically inferred for star-forming galaxies. Thus, these lines are essential for determining the effect of dust reddening, correcting all nebular emission lines for wavelength-dependent dust obscuration, and recovering the intrinsic nebular spectrum of a galaxy.

The $H\alpha/H\beta$ line ratio, or Balmer decrement, is by far the most commonly employed estimator of nebular dust reddening. The constituent lines are the strongest non-resonant recombination emission lines of hydrogen. They are simultaneously easily observed from the ground in certain redshift windows up to $z \sim 2.6$ (e.g., Förster Schreiber et al. 2009; Kashino et al. 2013; Reddy et al. 2015) and now with JWST, up to $z \sim 6.6$ (Shapley et al. 2023; Sandles et al. 2023; Clarke et al. 2024). They provide constraints on the dust attenuation towards the most massive stars and thus complement dust-reddening measures based on non-ionizing UV continuum emission (i.e., the UV spectral slope, β ; Calzetti et al. 1994; Meurer et al. 1999) or dust-reprocessed UV (i.e., IR) emission, while being less sensitive to star-formation history (Kennicutt et al. 1994). The latest generation of ground-based multi-object near-IR spectrographs (e.g., Keck/MOSFIRE, the Very Large Telescope (VLT)/KMOS) and space-based grism capabilities (e.g., the Hubble Space Telescope (HST)/WFC3 grism) have provided measurements of Balmer decrements for hundreds of galaxies up to $z \sim 2.6$ (e.g., Förster Schreiber et al. 2004; Kashino et al. 2013; Domínguez et al. 2013; Price et al. 2014; Reddy et al. 2015; Shivaei et al. 2020; Reddy et al. 2020; Fetherolf et al. 2021; Rezaee et al. 2021; Battisti et al. 2022; Lorenz et al. 2023), allowing for statistical analyses of nebular reddening, recombination-line-based SFRs, and gas-phase metallicities and ionization parameters from ratios of lines that are well separated in wavelength.

Such measurements are now possible well into the epoch of reionization owing to *JWST*'s unprecedented sensitivity, near-IR wavelength coverage, and spectral resolution (Shapley et al. 2023; Sandles et al. 2023), which allow for the detection of even weaker higher-order Balmer lines (e.g., $H\gamma$ up to $z \sim 10.5$, $H\delta$ up to $z \sim 11$). Even higher-fidelity measurements of nebular dust attenuation (and hence SFRs, gas-phase metallicities, and ionization parameters) can be achieved for intermediate-redshift galaxies where the Paschen lines lie within the wavelength coverage of NIR-Spec. The greater sensitivity and wavelength coverage offered by JWST naturally benefit studies of a large number of collisionally-excited and recombination nebular emission lines, allowing us to move beyond simple strong-line optical diagnostics (e.g., “BPT” diagrams; Baldwin et al. 1981) of the ISM, and perform simultaneous photoionization modeling of the full suite of rest-frame optical and near-IR nebular emission lines (e.g., Steidel et al. 2016; Topping et al. 2020; Reddy et al. 2022). Of course, the simultaneous modeling of many emission lines that are well separated in wavelength ne-

cessitates wavelength-dependent dust corrections that can be quantified by calculating the nebular dust attenuation curve.

The far more commonly studied stellar attenuation curve encapsulates the effects of dust absorption and scattering as determined by the composition of the dust grains, as well as the scattering of light into the line of sight, a nonuniform distribution of column densities, and spatial variations in optical depth within galaxies. The nebular attenuation curve captures these effects along the lines of sight towards the ionized regions, and hence the most massive stars, in galaxies, while the stellar attenuation curve generally applies to the stellar continuum contributed by all stars. Consequently, the stellar and nebular attenuation curves may differ depending on how the dust is distributed relative to stars of different masses. In particular, the main sequence lifetimes of the most massive O stars (spectral type O6 and earlier; Leitherer 1990) are shorter than the typical molecular cloud crossing timescale of $\lesssim 20$ Myr (Calzetti et al. 1994). Thus, while these stars are on the main sequence and dominating the ionizing flux, they are still embedded within their birth clouds and are found in regions of higher dust column density (c.f., Conroy & Kratzer 2012). Consequently, differences between the stellar and nebular dust attenuation curves may be expected if there are variations in dust grain size, absorption and scattering properties, spatial distribution, or column density between sightlines to massive O stars and sightlines to lower-mass stars contributing significantly to the non-ionizing UV continuum flux.

For starburst galaxies at high redshift, the Calzetti et al. (2000) and Small Magellanic Cloud (SMC; Gordon et al. 2003) curves are commonly assumed to describe the reddening of the stellar continuum, while the reddening towards the nebular regions is generally assumed to be described by the Galactic extinction curve (Cardelli et al. 1989). Constraining the stellar attenuation curve is generally more complex relative to the nebular attenuation curve. The former is highly model dependent, relying on assumptions about the intrinsic SED, which can vary considerably depending on the specifics of stellar population synthesis models and the star-formation history. In contrast, the nebular attenuation curve can be more straightforwardly constrained through photoionization modeling to deduce intrinsic H I recombination line ratios.

Using optical, mid-IR, and radio H I recombination lines detected for the local starburst galaxy, M82, Förster Schreiber et al. (2001) find a nebular reddening curve inconsistent with a foreground screen. They find that a mixed dust-stars model provides the best fit to the recombination lines. Using multiple Balmer emission lines ($H\alpha$, $H\beta$, $H\gamma$, $H\delta$, and $H\epsilon$) detected in ground-based composite spectra of a representative sample of $z \sim 2$ star-forming galaxies, Reddy et al. (2020) placed the first direct constraint on the nebular attenuation curve at high redshift (see Rezaee et al. 2021 for a similar analysis of nearby star-forming galaxies). They demonstrated that, on average, the shape of the curve at rest-frame optical wavelengths is similar to that of the Galactic extinction curve (Cardelli et al. 1989), the most commonly assumed curve describing nebular reddening (Calzetti et al.

1994). Prescott et al. (2022) used a combination of ground-based Balmer decrements and HST-based grism measurements of $\text{Pa}\beta$ for 11 galaxies at $z < 0.3$ to find a diversity of attenuation curve slopes and normalizations. These initial efforts to constrain the nebular attenuation curve underscored the need for deep observations over a wide baseline in wavelength, with well-characterized corrections for aperture (or slit) losses and/or relative flux calibration between different observational configurations to ensure accurate line ratios.

Initial surveys with JWST—e.g., the Cosmic Evolution Early Release Science survey (CEERS, Finkelstein et al. 2023), and the JWST Advanced Deep Extragalactic Survey (JADES, Eisenstein et al. 2023)—have demonstrated the transformative improvement in sensitivity, wavelength coverage, and spectral resolution necessary for *simultaneous* detections of the full range of Balmer and Paschen-series recombination emission lines for intermediate-redshift galaxies at $z \sim 1 - 4$. These surveys have enabled the first statistical analysis of nebular reddening and SFRs based on both Balmer and Paschen lines for the same galaxies at these redshifts (Reddy et al. 2023b). Now, with considerably higher S/N JWST/NIRSpec spectra collected for statistical samples of galaxies at intermediate redshifts, we can provide the most stringent constraints to date on the shape and normalization of the nebular attenuation curve for individual galaxies. Aside from allowing accurate nebular dust corrections on an individual object-by-object basis, these datasets enable us to examine the scatter in the nebular attenuation curve and its effect on other commonly-derived quantities such as ionization parameters, metallicities, and star-formation rates.

Here we take advantage of the deep near-IR spectroscopy provided by the Cycle 1 JWST/NIRSpec program “The Assembly of Ultradeep Observations Revealing Astrophysics” (AURORA, PID:1914). This survey was designed to detect faint auroral emission lines from ionized O, S, and N in $z > 1.4$ galaxies, with the aim of measuring electron temperatures and obtaining direct estimates of O abundance, independent of “strong-line” estimates of gas-phase metallicity which suffer from a number of systematic uncertainties. As a result of the required depth to detect the weak auroral lines, AURORA spectra represent a marked improvement in S/N for typical star-forming galaxies at intermediate redshifts compared to earlier surveys (e.g., CEERS). In particular, these spectra include the robust detection of many of the weaker higher-order Balmer and Paschen-series emission lines over the continuous wavelength range of $1 - 5 \mu\text{m}$, along with significant S/N in the stellar continuum that aids in the relative flux calibration between gratings, thus obviating much of the systematic uncertainty in flux calibration between measurements obtained with different telescopes and instruments and in different weather conditions (e.g., Prescott et al. 2022). Using the AURORA spectroscopy, Sanders et al. (2024) adopt the methodology laid out in Reddy et al. (2020) to constrain the shape of the nebular dust attenuation curve for a young $z = 4.411$ galaxy, GOODS-N-17940, finding a curve that deviates significantly in shape from the Galactic extinction curve. Fully quantifying the diversity in the shape and

normalization of the nebular dust attenuation curve requires a statistical analysis of objects spanning a range of galaxy properties (e.g., SFR, stellar mass, gas-phase abundance) that are known to correlate with dust attenuation. To that end, in this paper we use the deep NIRSpec spectroscopy from the AURORA survey to provide the first robust constraints on the nebular reddening and the nebular attenuation curve for a statistical sample of individual galaxies based on multiple Balmer and Paschen emission lines. We further demonstrate how the detection of multiple H I recombination lines can provide novel constraints on the dust covering fraction toward OB associations.

The paper is organized as follows. The AURORA survey, data reduction, slitloss corrections, primary measurements, and sample selection are outlined in Section 2. The comparison between the Balmer-inferred and Paschen-inferred nebular reddening is presented in Section 3. Section 4 builds on previous work (e.g., Reddy et al. 2020; Rezaee et al. 2021) by focusing on the derivation of nebular dust attenuation curves for individual galaxies. Finally, Section 5 explores a more sophisticated model that allows for a sub-unity covering fraction of dust in order to simultaneously reproduce the observed H I Balmer and Paschen recombination line ratios. The broader implications of the nebular dust attenuation curves in terms of dust-corrected line luminosities and line ratios, SFRs, and differential reddening of the nebular lines and stellar continuum, are presented in a separate paper, hereafter Paper II (Reddy et al., submitted). A Chabrier (2003) initial mass function (IMF) is considered throughout the paper. Wavelengths are reported in the vacuum frame. We adopt a cosmology with $H_0 = 70 \text{ km s}^{-1} \text{ Mpc}^{-1}$, $\Omega_\Lambda = 0.7$, and $\Omega_m = 0.3$.

2. DATA AND MEASUREMENTS

2.1. Observations and Spectral Data Reduction

The JWST/NIRSpec spectroscopy used in this analysis was drawn from the AURORA survey (PID: 1914, co-PIs: Shapley and Sanders). The central strategy of the survey was to target the auroral lines of multiple elements (O, N, and S) for individual galaxies at $z > 1.4$, with the aim of constraining their electron temperatures and obtaining direct O abundances. The survey targeted 46 and 51 galaxies, respectively, in the COSMOS and GOODS-N fields. Details of the target selection are provided in Shapley et al. (2025). The G140M/F100LP, G235M/F170LP, and G395M/F290LP grating/filter combinations were used, providing $R \sim 1000$ spectroscopy over the full wavelength range spanning 1 to $5 \mu\text{m}$. A three-dither nodding pattern was used and the total integration times in the three grating/filter combinations for each pointing were 12.3, 8.0, and 4.2 hrs, respectively, yielding a uniform 3σ line flux detection limit of $5 \times 10^{-19} \text{ erg s}^{-1} \text{ cm}^{-2}$ from 1 to $5 \mu\text{m}$.

The standard STScI NIRSpec data reduction pipeline and custom software developed for the AURORA survey were used to process the raw data and obtain flat-fielded and wavelength-calibrated two-dimensional (2D) spectrograms. Optimal extraction was used to create one-dimensional (1D)

science and error spectra from the 2D spectrograms, using a spatial profile determined by the brightest emission line in each grating, or the integrated continuum profile if no emission lines were detected. Only for $\sim 1\%$ of the targets was a blind extraction performed. Further details on the survey parameters, including target selection and data reduction, can be found in [Shapley et al. \(2025\)](#).

2.2. Slit Loss Corrections and Flux Calibration

Owing to the small spatial scale of the NIRSpec MSA microshutter ($0''.20 \times 0''.46$) relative to the typical size of the targeted galaxies, a substantial fraction of the light from these galaxies falls outside the spectroscopic aperture. This issue is particularly acute for galaxies significantly offset from the center of the microshutter. To correct for the light lost outside the aperture, one must account for the aperture size, the intrinsic size of the galaxy, any offset of the galaxy within the aperture, and the wavelength-dependent point-spread function (PSF).

The methodology used to correct for this “slit loss” follows that of [Reddy et al. \(2023b\)](#). Specifically, a $12'' \times 12''$ subimage centered on the target was extracted from the NIRCam F115W imaging. Using the segmentation map, pixels corresponding to unrelated objects were masked. The subimage was then rotated to account for the position angle of the NIRSpec observations, and convolved with Gaussian kernels to simulate the expected light profiles at longer wavelengths. These kernels were calculated by subtracting in quadrature the FWHM of the JWST PSF at $1.15 \mu\text{m}$ from the FWHMs of the JWST PSFs at $\lambda = 1.2 - 5.3 \mu\text{m}$, in increments of $\Delta\lambda = 0.1 \mu\text{m}$.

For four objects in COSMOS and two in GOODS-N that lacked NIRCAM F115W imaging, Sérsic fits from the HST/WFC3 F160W images, as presented in ([van der Wel et al. 2014](#)), were used to model the galaxies. These models were then convolved with the JWST PSFs at $\lambda = 0.6 - 5.3 \mu\text{m}$, in increments of $\Delta\lambda = 0.1 \mu\text{m}$, generated using the JWST WebbPSF software.¹ Additionally, for five targets in GOODS-N, which did not have reliable Sérsic fits or F115W imaging, a point-source model was assumed.

The above procedure generates convolved images of the galaxy at each wavelength. These images were shifted according to the target’s offset from the microshutter center and then masked. The masking accounts for the $0''.20$ microshutter width, the $0''.07$ gap between adjacent microshutters along the cross-dispersion axis, and the window used to extract the 1D spectra from the 2D spectrograms. The 1D spectra were corrected for slitloss by dividing them by the fraction of light transmitted within the spectroscopic and extraction apertures as a function of wavelength.

The impact of the slitloss corrections is illustrated in Figure 1, which shows that the fraction of transmitted light as a function of wavelength typically decreases by $\simeq 10\%$ from

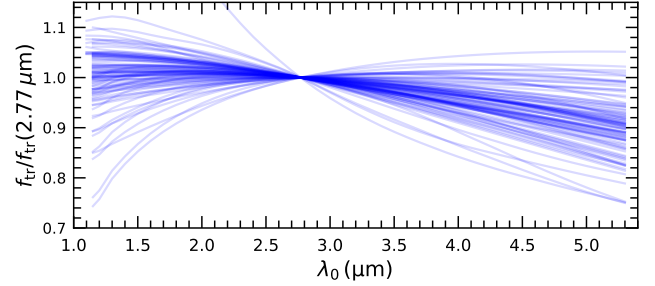


Figure 1. Fraction of transmitted flux as a function of wavelength, normalized by the fraction of transmitted flux at $2.77 \mu\text{m}$, for the 96 galaxies in the AURORA parent sample.

$\lambda_0 = 1$ to $5 \mu\text{m}$. However, for some galaxies that contain subcomponents that are substantially off-center, the widening of the PSF can increase the fraction of transmitted flux at longer wavelengths.

The final flux calibration of the spectra involved two steps. First, the G140M and G395M spectra were scaled using the G235M grating spectra as a reference, ensuring that the line fluxes and continuum flux densities in overlapping wavelength regions matched. This step is facilitated by the deep AURORA spectra, which provide high S/N detections of the continua for all galaxies relevant to our analysis. Second, an absolute flux calibration was performed by scaling the spectra to match the available multi-wavelength photometry. Further details on the relative and absolute flux calibrations can be found in [Sanders et al. \(2024\)](#).

2.3. Line Measurements

Emission-line flux measurements were performed by fitting a single Gaussian function to well-isolated lines, or multiple Gaussians for lines closely separated in wavelength. In fitting the lines, the continuum was initially defined by the best-fit SED model (Section 2.4) to the multi-wavelength photometry, prior to the application of any corrections for emission lines or nebular continuum. The resulting emission-line measurements were then used to correct the multi-wavelength photometry. The continuum from the best-fit SED model to this corrected photometry was subsequently used to refit all the lines and obtain the final flux measurements. Because the continuum is defined by the best-fit SED model, the final flux measurements for the H I recombination lines account for underlying stellar absorption. This effect is most significant for the higher-order Balmer lines, where the absorbed flux relative to the emission-line flux is more pronounced.

2.4. SED Fitting

The COSMOS and GOODS-N fields contain publicly available photometry from JWST/NIRCam and HST/ACS and WFC3, which were obtained from the Dawn JWST Archive (DJA; [Valentino et al. 2023](#); [Heintz et al. 2025](#)). In COSMOS, the bands include the following: F435W, F606W, F814W, F850LP, F105W, F125W, F140W, and F160W from

¹ <https://www.stsci.edu/jwst/science-planning/proposal-planning-toolbox/psf-simulation-tool>

HST; and F090W, F115W, F150W, F200W, F277W, F356W, F410M, and F444W from JWST/NIRCam. In GOODS-N, the bands include the following: F435W, F606W, F775W, F814W, F850LP, F105W, F125W, F140W, and F160W from HST; and F090W, F115W, F150W, F182M, F200W, F210M, F277W, F335M, F356W, F410M, and F444W from JWST/NIRCam. For four sources in COSMOS that do not contain JWST/NIRCam imaging, photometry from the 3D-HST catalog was used (Skelton et al. 2014). Details on how the photometry was performed are given in Valentino et al. (2023).

The photometry was used to model the stellar populations of the galaxies, yielding estimates of SFRs, ages, continuum reddening ($E(B - V)_{\text{cont}}$), and stellar masses. The Binary Population and Spectral Synthesis (BPASS) version 2.2.1 models (Eldridge et al. 2017; Stanway & Eldridge 2018) were considered for this purpose. We assumed constant star-formation models that include the effects of binary stellar evolution; ages ranging from 1 Myr to the age of the Universe at the redshift of each galaxy; a stellar metallicity of $Z_* = 0.001$ (corresponding to $Z_* \simeq 1/10 Z_\odot$), based on previous constraints on Z_* for other galaxies at the same redshifts (e.g., Steidel et al. 2016; Cullen et al. 2019; Topping et al. 2020; Reddy et al. 2022; Kashino et al. 2022; Chartab et al. 2024); and a $100 M_\odot$ cutoff of the IMF. Finally, the SMC extinction curve was assumed for the reddening of the stellar continuum, again based on previous results (e.g., Reddy et al. 2006; Shivaie et al. 2015; Bouwens et al. 2016; Fudamoto et al. 2017; Reddy et al. 2018a,b; Theios et al. 2019; Reddy et al. 2022). For the purposes of this analysis, the best-fit SEDs are only used for measuring emission-line fluxes (Section 2.3), so the results are insensitive to the particular choice of star-formation history and reddening curve.²

2.5. Final Sample Selection

Of the 94 galaxies with spectroscopic redshifts in the parent AURORA sample, we culled a subsample suitable for the present analysis. First, 8 AGN and quiescent galaxies were excluded based on prior known information for these sources (see Shapley et al. 2025), and inspection of the SEDs and/or AURORA spectra for signatures of broad lines or lack of emission lines. Second, 9 objects where the flux calibration was suspect due to inconsistent line ratios between adjacent gratings or inconsistent/unphysical line ratios within the same grating were removed. Third, 2 galaxies exhibiting observed line ratios inconsistent with Case B recombination were removed. Fourth, to ensure robust constraints on the nebular dust attenuation curve, 4 galaxies which have a negligible reddening based on the Balmer lines were removed. Fifth, we removed 34 galaxies at higher redshifts which did not have coverage of any Paschen lines. Finally, we required

$> 5\sigma$ detections of at least 5 lines, at least 2 of which must be Paschen lines, resulting in the exclusion of 13 additional galaxies. Applying the above criteria yielded a sample of 24 galaxies, each having anywhere from 5 to 16 5σ detections of the H I Balmer and Paschen recombination lines, with a median of 11 lines. Figure 2 shows the 2D and 1D spectra of one of the objects in the sample, GOODS-N-30564, which has 9 detected Balmer lines and 5 detected Paschen lines. The redshift distributions of the parent AURORA sample and the final sample of 24 galaxies used for this analysis are shown in Figure 3. In addition to the 24 galaxies in the primary sample, we also consider in Section 4.3 additional galaxies, many at $z \gtrsim 4$, that did not have more than two detected Paschen lines.

Figure 4 shows the distributions of the observed $H\alpha$ luminosities and Balmer decrements for the parent AURORA sample with $> 5\sigma$ detections of $H\alpha$ and $H\beta$, along with the same distributions for the subsample of 24 galaxies that satisfy the aforementioned selection criteria. Not surprisingly, the median Balmer decrement is higher for the subsample of 24 galaxies ($H\alpha/H\beta \simeq 3.6$ vs 3.3 for the parent sample) since we only included galaxies where the Balmer lines indicate non-negligible reddening. The additional requirement of the detection of at least 2 Paschen lines with $S/N > 5$ results in a subsample with a median observed $H\alpha$ luminosity that is $\simeq 0.4$ dex larger than that of the parent sample.

3. NEBULAR REDDENING FROM THE BALMER AND PASCHEN LINES

The longer-wavelength Paschen lines are less affected by dust attenuation than the Balmer lines and can thus provide an independent probe of the intrinsic H I recombination line luminosities. As we show below, the combination of the Balmer and Paschen lines provides the most stringent constraints on not only the nebular reddening, but also the shape and normalization of the nebular attenuation curve. For the moment, we focus on the nebular reddening derived from the Balmer and Paschen line ratios adopting the commonly-assumed Galactic extinction curve of Cardelli et al. (1989). The observed flux of a line at wavelength λ , $f(\lambda)$, can be expressed as a function of the intrinsic flux of that line, $f_0(\lambda)$, the nebular reddening, $E(B - V)_{\text{neb}}$, and the nebular attenuation curve, k_{neb} :

$$f(\lambda) = f_0(\lambda) \times 10^{-0.4E(B-V)_{\text{neb}}k_{\text{neb}}(\lambda)}. \quad (1)$$

The ratio of the observed fluxes of two lines at wavelengths λ_1 and λ_2 can then be written as

$$\frac{f(\lambda_1)}{f(\lambda_2)} = \frac{f_0(\lambda_1)}{f_0(\lambda_2)} \times 10^{-0.4E(B-V)_{\text{neb}}[k_{\text{neb}}(\lambda_1) - k_{\text{neb}}(\lambda_2)]}. \quad (2)$$

Defining

$$R \equiv \log_{10} \left[\frac{f(\lambda_1)}{f(\lambda_2)} \right] - \log_{10} \left[\frac{f_0(\lambda_1)}{f_0(\lambda_2)} \right], \quad (3)$$

we can write

$$R = -0.4E(B - V)_{\text{neb}}[k_{\text{neb}}(\lambda_1) - k_{\text{neb}}(\lambda_2)]. \quad (4)$$

² The random uncertainties (tied to photometric errors) and systematic uncertainties (associated with assuming a different stellar reddening curve or star-formation history) in the Balmer absorption corrections are negligible and do not affect the measured emission-line fluxes (e.g., see Reddy et al. 2015 for further details).

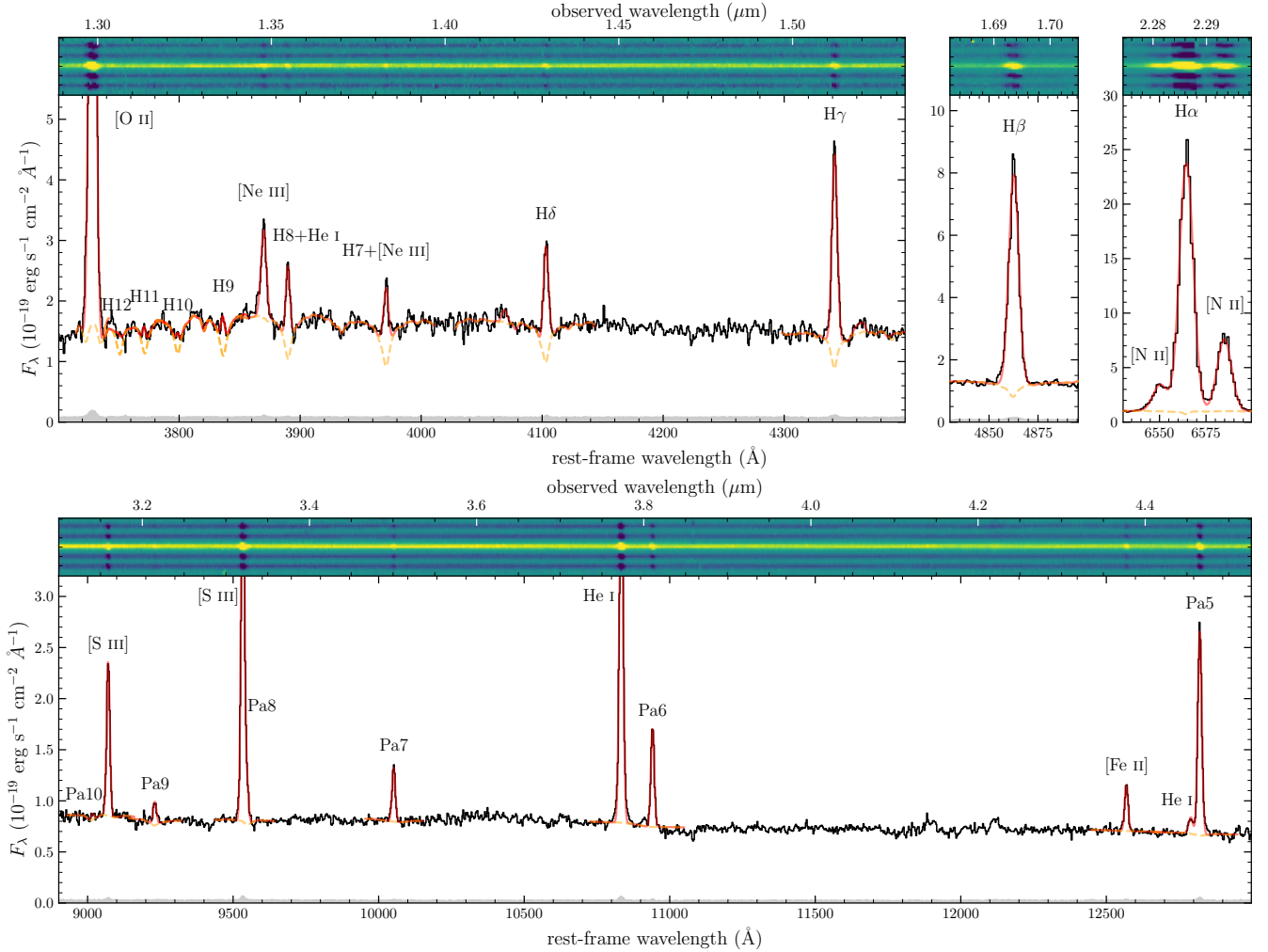


Figure 2. Two- and one-dimensional JWST/NIRSpec spectra of one of the objects in the main sample, GOODS30564 ($z = 2.4828$), showing the detection of multiple H I Balmer and Paschen emission lines. The 1D spectrum is shown in black, and the error spectrum is indicated in grey. The underlying stellar continuum and fits to the emission lines are shown in orange and red, respectively.

The observed and intrinsic line ratios and an assumed nebular attenuation curve can then be used to calculate the nebular reddening using Equations 3 and 4.

Intrinsic H I recombination line ratios were obtained from PyNeb (Luridiana et al. 2015) with an electron density $n_e = 100 \text{ cm}^{-3}$ and temperature $T = 15,000 \text{ K}$. This n_e is within a factor of $\simeq 3$ of the typical densities found in galaxies at $z \sim 2-3$, as indicated by both ground-based spectroscopy of samples spanning similar redshifts (e.g., Steidel et al. 2014, 2016; Sanders et al. 2016; Strom et al. 2017; Topping et al. 2020; Reddy et al. 2023c) and, more recently, with JWST spectroscopy of galaxies at the same redshifts (e.g., Reddy et al. 2023a; Isobe et al. 2023; Topping et al. 2025). The impact of varying n_e within the range inferred for star-forming galaxies ($n_e < 10^4 \text{ cm}^{-3}$) on the intrinsic line ratios is negligible. However, a factor of ≈ 2 variation in temperature at a fixed n_e can cause non-negligible shifts in line ratios, particularly for the higher-order Balmer lines and the Paschen lines (e.g., Ferguson & Ferland 1997). Appendix A summa-

rizes the variations in the line ratios obtained at different temperatures. The appendix further presents different treatments of angular-momentum-state mixing (or l -mixing) in various principle quantum (n) states and the impact on the intrinsic line ratios, which ultimately influences the derived shape of the nebular dust attenuation curve. For ease of reference, the default PyNeb values mentioned above yield the intrinsic line ratios listed in Table 1, which are adopted for the subsequent analysis.

To get a sense for how robustly $E(B - V)_{\text{neb}}$ can be constrained with the Balmer and Paschen lines, we show in Figure 5 R versus rest-frame wavelength (λ_0) for $E(B - V)_{\text{neb}} = 0.1 - 1.0$ in increments of $\delta E(B - V)_{\text{neb}} = 0.1$ assuming the Cardelli et al. (1989) curve, where the reference wavelength (i.e., λ_2 in Equation 3) is taken to be that of Pa4 (Pa α). Due to the shallower wavelength dependence of the Cardelli et al. (1989) curve, and attenuation curves in general, with increasing wavelength, the longer-wavelength

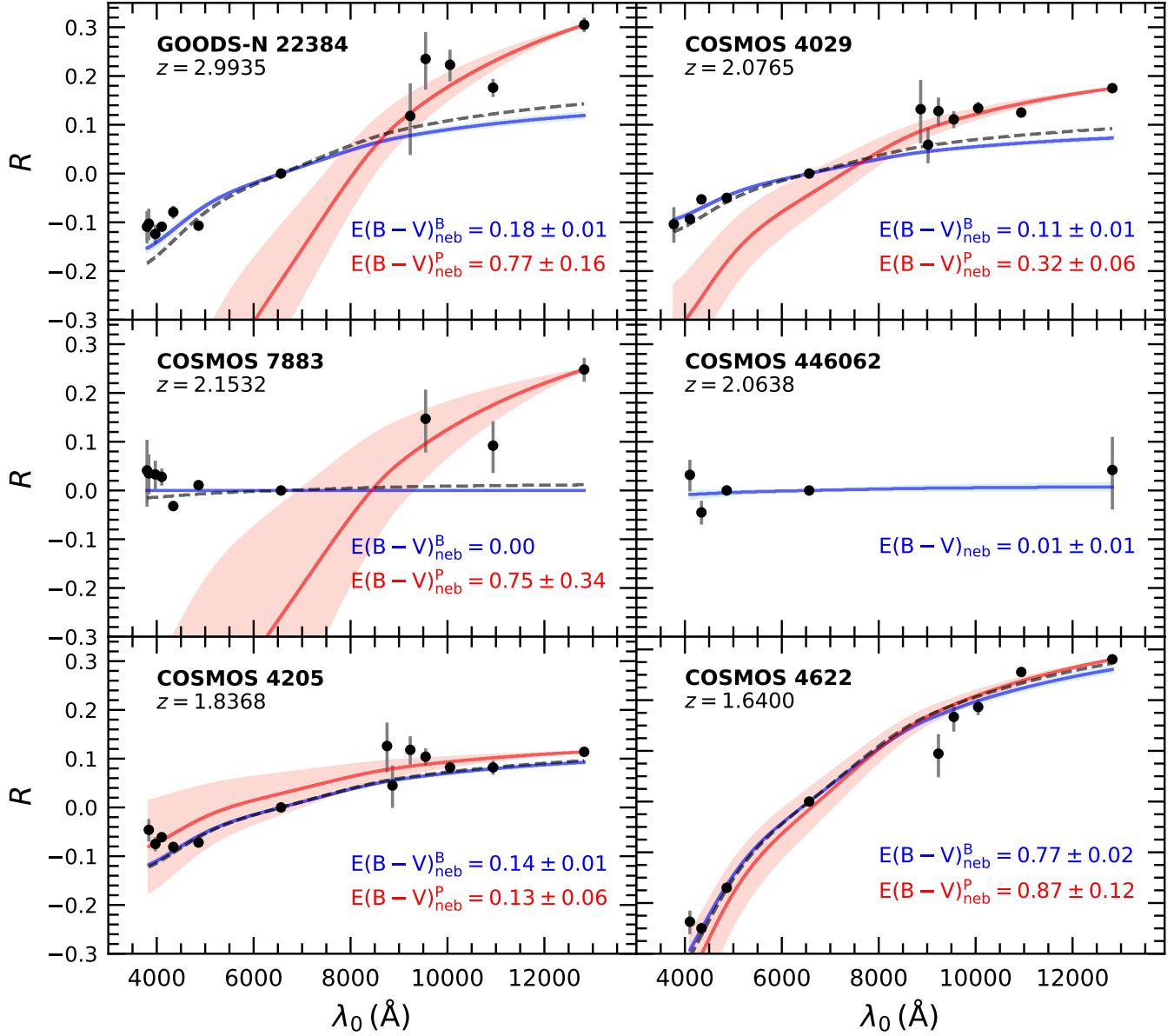


Figure 6. R versus rest-frame wavelength for a representative subsample of 6 galaxies. The measured values and uncertainties in R are indicated by the black points and errorbars. The predicted relationship between R and λ_0 for the $E(B - V)_{\text{neb}}$ that best fits the Balmer lines only and the Paschen lines only, are shown by the blue and red curves, respectively, while the shaded regions indicate the 68% confidence intervals in the fits. The dashed lines indicate the same when fitting all available lines. R is computed with $H\alpha$ as the reference line, and the predictions shown here assume the [Cardelli et al. \(1989\)](#) extinction curve. The best-fit $E(B - V)_{\text{neb}}^{\text{B}}$ and $E(B - V)_{\text{neb}}^{\text{P}}$ are indicated in each panel. The two objects shown in the middle row (COSMOS 7883 and COSMOS 446062) are not among the 24 galaxies in the main sample since they have $E(B - V)_{\text{neb}}^{\text{B}} = 0$. The sample includes a mix of galaxies, some with comparable Balmer and Paschen inferred reddening, some where the Paschen inferred reddening exceeds that from the Balmer lines, and some where all the lines indicate negligible nebular reddening.

Table 1. Intrinsic H I Recombination Line Emissivities Relative to H α

Line	λ (Å) ^a	I^b
H12	3751.22	0.01106
H11	3771.70	0.01440
H10	3798.98	0.01925
H9	3836.48	0.02657
H8 ^c	3890.17	0.03819
H7 ^d	3971.20	0.05783
H δ	4102.89	0.0941
H γ	4341.68	0.16960
H β	4862.68	0.35863
H α	6564.61	1.00000
Pa16	8504.83	0.00154
Pa15	8547.73	0.00186
Pa14	8600.75	0.00229
Pa13	8667.40	0.00287
Pa12	8752.86	0.00365
Pa11	8865.32	0.00475
Pa10	9017.77	0.00634
Pa9	9232.23	0.00875
Pa8	9548.82	0.01255
Pa7	10052.56	0.01897
Pa6	10941.17	0.03070
Pa5	12821.58	0.05459
Pa4	18756.42	0.10930

^a Rest-frame vacuum wavelength.

^b Intensity of line relative to H α for Case B recombination, $T_e = 15,000$ K, and $n_e = 100 \text{ cm}^{-3}$, taken from PyNeb.

^c H8 is blended with He I $\lambda 3890$ and was not used in the analysis.

^d H7 (He) is blended with [Ne III] $\lambda 3969$. The contribution of the latter to the total line flux was calculated by multiplying the measured [Ne III] $\lambda 3870$ flux by 0.31 (Section 2.3).

Paschen lines alone is generally larger than that obtained from the Balmer lines. The dashed lines in each panel indicate the fit to all available lines, which, due to the high S/N (and relatively high weighting) of the Balmer lines, yields an $E(B - V)_{\text{neb}}$ that is close to $E(B - V)_{\text{neb}}^B$. The top two panels of Figure 6 show two galaxies where the $E(B - V)_{\text{neb}}$ obtained from the Balmer lines alone is lower than that obtained from the Paschen lines alone. For example, for GOODS-N 22384, R normalized to H α results in a fit to the Balmer lines that underpredicts the Pa5 (Pa β) line flux by $\simeq 0.2$ dex.

For the same galaxy, R normalized to Pa5 yields a fit to the Paschen lines that underestimates the higher order Balmer line fluxes (i.e., H γ and higher) by $\gtrsim 0.3$ dex.

The middle left panel shows another galaxy (COSMOS-7883) where the Balmer lines indicate little to no reddening, while the Paschen lines indicate considerable reddening. This example underscores the potential danger in assuming little nebular reddening or dust attenuation based on the Balmer lines alone. For the three galaxies discussed above, it is evident that the Cardelli et al. (1989) curve cannot simultaneously reproduce all the line ratios with a single value of $E(B - V)_{\text{neb}}$. This apparent discrepancy can be resolved if the dust optical depth is sufficiently large such that the emission dominating the Balmer lines comes from regions of lower optical depth relative to the Paschen lines. We return to this point below.

The middle right panel of Figure 6 shows R versus λ_0 for a galaxy where the Balmer lines and the single Paschen line with $S/N \geq 5$ (Pa5) indicate little or no reddening. The bottom two panels show galaxies where the reddening derived from the Balmer and Paschen lines are consistent with each other. Thus, the AURORA sample contains a mix of galaxies, some where $E(B - V)_{\text{neb}}^B < E(B - V)_{\text{neb}}^P$, others where $E(B - V)_{\text{neb}}^B \simeq E(B - V)_{\text{neb}}^P$, and some where $E(B - V)_{\text{neb}} \simeq 0$.

A comparison of $E(B - V)_{\text{neb}}^B$ and $E(B - V)_{\text{neb}}^P$ assuming the Galactic extinction curve for all 24 galaxies in the final sample (Figure 7) shows that 13 of them have $E(B - V)_{\text{neb}}^B < E(B - V)_{\text{neb}}^P$ at the $\leq 1\sigma$ level. The SMC (Gordon et al. 2003) extinction curve or the Calzetti et al. (2000) attenuation curve results in 10 and 11 galaxies, respectively, having $E(B - V)_{\text{neb}}^B < E(B - V)_{\text{neb}}^P$ at the $\leq 1\sigma$ level. These curves have a very similar shape to the Galactic extinction curve at the wavelengths of the Balmer lines, resulting in $E(B - V)_{\text{neb}}^B$ that are on average 0.01 and 0.03 mag bluer than those derived with the Galactic extinction curve. At the wavelengths of the Paschen lines, the SMC and Calzetti curves are somewhat steeper than the Galactic extinction curve, returning $E(B - V)_{\text{neb}}^P$ that are on average 0.10 and 0.17 mag bluer than those derived with the Galactic extinction curve. In any case, regardless of which extinction or attenuation curve is assumed, we find that roughly half of the galaxies have nebular reddening derived from the Paschen lines that is systematically larger than that derived from the Balmer lines. These findings are consistent with previous investigations that suggested redder $E(B - V)_{\text{neb}}$ derived from Paschen lines relative to Balmer lines (Prescott et al. 2022; Giménez-Arteaga et al. 2022; Reddy et al. 2023b).

Formally, there are four galaxies where the Paschen lines alone indicate negligible reddening, while the Balmer lines indicate substantial reddening. In these cases, the Paschen line ratios have sufficiently large uncertainties and/or scatter about the expected intrinsic values, and thus do not provide sufficient leverage to independently constrain the reddening. For all four galaxies, the combination of any of the Paschen lines and one or more Balmer lines indicates non-zero red-

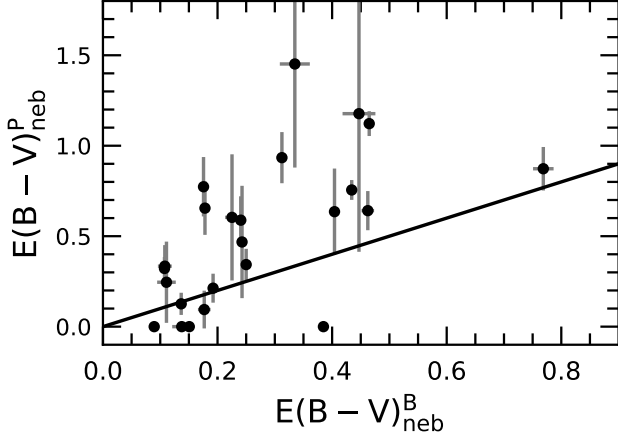


Figure 7. Comparison of $E(B - V)_{\text{neb}}^B$ and $E(B - V)_{\text{neb}}^P$ for the 24 galaxies in the final sample. The line of equality is indicated in black.

dening. Thus, regardless of the choice of attenuation curve, we do not find significant evidence for galaxies where the Balmer-derived reddening is *larger* than the reddening derived using a combination of the Balmer and Paschen lines, consistent with previous studies (Prescott et al. 2022; Reddy et al. 2023b).

4. THE EFFECTIVE ATTENUATION CURVE

As noted in the previous section, the assumption of the Galactic or SMC extinction curves, or the Calzetti attenuation curve, results in discrepancies between the Balmer and Paschen-inferred reddening for at least half the galaxies in the sample. This result suggests that the nebular dust attenuation curves deviate from the typically-assumed Galactic extinction curve, and other common extinction and attenuation curves (Förster Schreiber et al. 2001; Prescott et al. 2022; Sanders et al. 2024). The effective attenuation curve—or, alternatively, the arbitrarily normalized effective attenuation curve, or “relative” attenuation curve—can be calculated using the methodology first introduced in Reddy et al. (2020), and presented in Section 4.1. Section 4.2 discusses the attenuation curves derived for individual galaxies, as well as the average curve computed for the sample. The latter can be useful when applying dust corrections to populations of galaxies. The consistency of this average attenuation curve with the recombination line ratios of galaxies outside the main sample, including those at $z > 3$, is explored in Section 4.3. Constraints on the normalization of the nebular attenuation curve are described in Section 4.4.

4.1. Methodology

The attenuation in magnitudes at wavelength λ can be expressed in terms of the nebular reddening and the nebular dust attenuation curve:

$$A_{\text{neb}}(\lambda) = E(B - V)_{\text{neb}} k_{\text{neb}}(\lambda). \quad (5)$$

Equation 2 can then be written in terms of $A_{\text{neb}}(\lambda)$:

$$\frac{f(\lambda_1)}{f(\lambda_2)} = \frac{f_0(\lambda_1)}{f_0(\lambda_2)} \times 10^{-0.4[A_{\text{neb}}(\lambda_1) - A_{\text{neb}}(\lambda_2)]}, \quad (6)$$

or

$$A_{\text{neb}}(\lambda_2) = 2.5 \left[\log_{10} \left(\frac{f(\lambda_1)}{f(\lambda_2)} \right) - \log_{10} \left(\frac{f_0(\lambda_1)}{f_0(\lambda_2)} \right) \right] + A_{\text{neb}}(\lambda_1). \quad (7)$$

Following Reddy et al. (2020), we can define a new quantity that depends only on the measured and intrinsic line ratios:

$$\begin{aligned} A'_{\text{neb}}(\lambda_2) &\equiv A_{\text{neb}}(\lambda_2) + [1 - A_{\text{neb}}(\lambda_1)] \\ &= 2.5 \left[\log_{10} \left(\frac{f(\lambda_1)}{f(\lambda_2)} \right) - \log_{10} \left(\frac{f_0(\lambda_1)}{f_0(\lambda_2)} \right) \right] + 1. \end{aligned} \quad (8)$$

Given Equation 5, the relative attenuation curve can be written as

$$k'_{\text{neb}}(\lambda) = \frac{A'_{\text{neb}}(\lambda)}{A'_{\text{neb}}(B) - A'_{\text{neb}}(V)}, \quad (9)$$

where we have set $\lambda = \lambda_2$ and used the definition that $E(B - V)_{\text{neb}} = A_{\text{neb}}(B) - A_{\text{neb}}(V)$.

$A'_{\text{neb}}(\lambda)$ was calculated for each of the 24 galaxies in the sample based on the observed and intrinsic line ratios using $H\alpha$ as the reference line (λ_1). A fifth-order polynomial was then fit to $A'_{\text{neb}}(\lambda)$ versus $\mu = 1/\lambda$. For some objects in the sample, the noisier higher-order Balmer lines can result in a non-monotonic polynomial fit to $A'_{\text{neb}}(\lambda)$. To enforce monotonicity, this polynomial was constrained to have a derivative that is a perfect square (i.e., the square of a quadratic function). This requirement of monotonicity implies that the fit has 4 (rather than 6) degrees of freedom. The fit was used to calculate $A'_{\text{neb}}(B)$ and $A'_{\text{neb}}(V)$, where we adopt 4400 Å and 5500 Å, respectively, for the effective wavelengths of the B and V bands. The $A'_{\text{neb}}(\lambda)$ data points and polynomial fit were then divided by $A'_{\text{neb}}(B) - A'_{\text{neb}}(V) = E(B - V)_{\text{neb}}^{\text{eff}}$ to calculate $k'_{\text{neb}}(\lambda)$. With the previous definitions, $k'_{\text{neb}}(\lambda)$ is equivalent to $k_{\text{neb}}(\lambda)$ up to a normalization constant. For the remainder of the analysis, $k'_{\text{neb}}(\lambda)$ was shifted so that $k'_{\text{neb}}(V) = 0$, thus implying that

$$k_{\text{neb}}(\lambda) = k'_{\text{neb}}(\lambda) + R_V, \quad (10)$$

where R_V is the value of the total attenuation curve at V -band (5500 Å). The normalization constant, R_V , is discussed further in Section 4.4.

4.2. Individual and Average Relative Nebular Attenuation Curves

Figure 8 shows $k'_{\text{neb}}(\lambda)$ as a function of wavelength for four representative galaxies in the sample. Also shown for comparison are the Galactic and SMC extinction curves, and the Calzetti attenuation curve, all shifted so that their value at V -band is zero. The $k'_{\text{neb}}(\lambda)$ for individual galaxies show

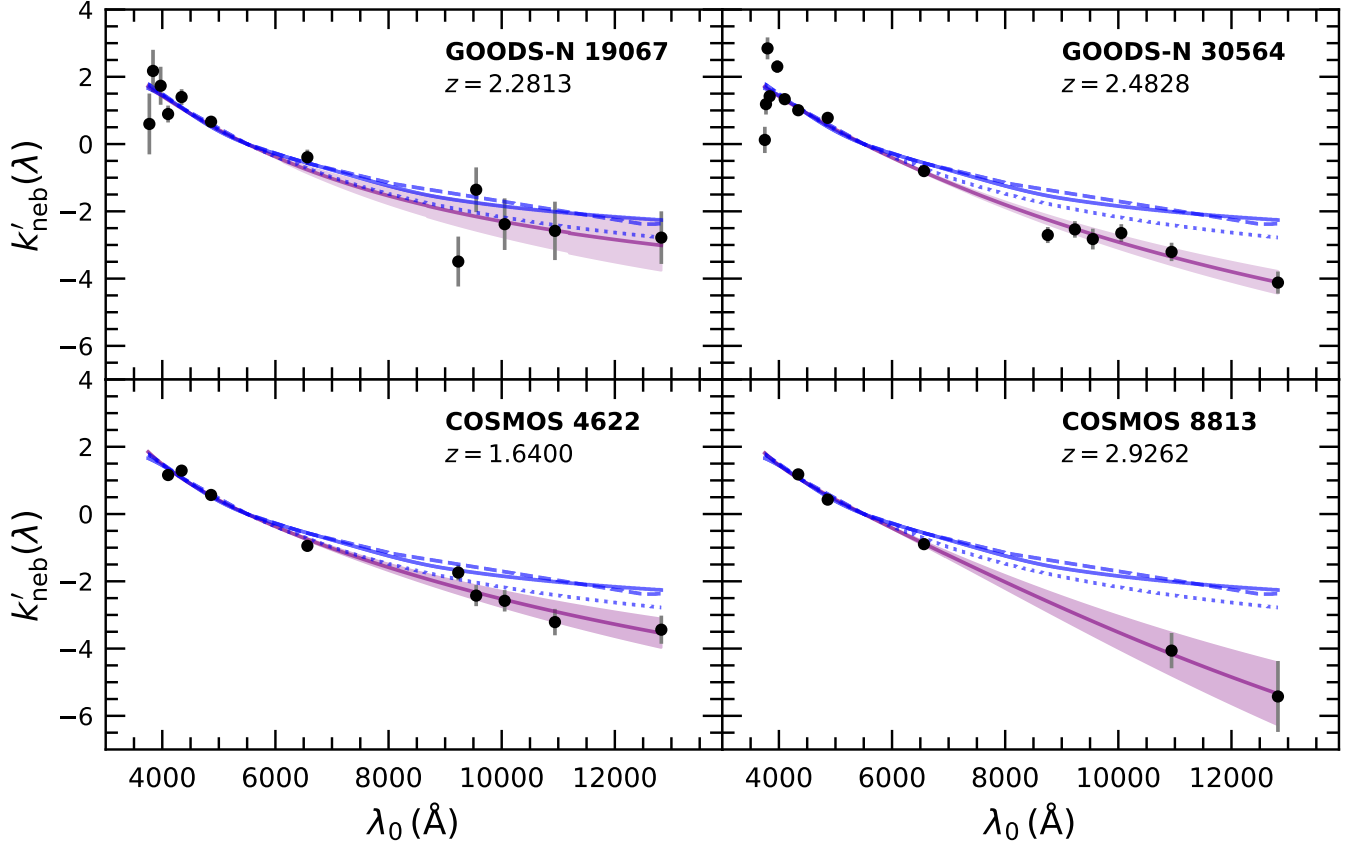


Figure 8. $k'_{\text{neb}}(\lambda)$ versus λ_0 for four galaxies in the sample, with the best-fit fifth-order polynomials and 1σ confidence intervals shown by the purple lines and shaded regions, respectively. Also shown in each panel are the Galactic, SMC, and Calzetti curves (solid, dotted, and dashed blue lines, respectively), shifted so that they pass through zero at 5500 \AA .

a diversity of shapes, from ones that are essentially identical in shape to other commonly-adopted extinction and attenuation curves (GOODSN-19067), to ones that deviate markedly in shape from the common curves at $\lambda \gtrsim 8000 \text{ \AA}$ (e.g., GOODSN-30564 and COSMOS-8813).

The inability to simultaneously reproduce all the Balmer and Paschen line ratios with the commonly-adopted extinction or attenuation curves for most of the galaxies in the sample, as discussed in Section 3, suggests effective attenuation curves that differ in shape from the commonly adopted ones. This effect can be seen directly in Figure 8, where the curves of three of the four galaxies shown (GOODSN-30564, COSMOS-4622, and COSMOS-8813) have a steeper dependence on wavelength, particularly at near-IR wavelengths, than the Galactic, SMC, and Calzetti curves. This behavior cannot be attributed to inaccuracies in the relative flux calibration between adjacent gratings. Specifically, as noted in Section 2.2, all galaxies in the sample have significantly detected continua and/or emission lines in the overlap regions between gratings, allowing for accurate relative flux calibration. Additionally, 10 galaxies that show attenuation curves that deviate from the Galactic extinction curve have one or more Paschen lines in the same grating as $\text{H}\alpha$. Finally, the wavelength-dependent slitloss corrections inferred

from the transmission curves described in Section 2.2 result in a relative shift between $k'(\lambda)$ at the wavelengths of $\text{H}\alpha$ and Pa5 of $\Delta k'(\lambda) \simeq 0.27$ on average. This shift is considerably smaller than the typical deviation of $k'(\lambda)$ from the value predicted by the Galactic extinction curve at the wavelength of Pa5 (Figure 8). Therefore, the deviations observed in the attenuation curves, when compared to other standard extinction or attenuation curves, cannot be ascribed to flux calibration uncertainties between gratings or uncertainties in slitloss corrections. Instead, these deviations are likely to be of a physical nature.

For the galaxies shown in Figure 8, the shapes of the curves at $\lambda \lesssim 5500 \text{ \AA}$ (spanning the wavelength range of all the Balmer lines except $\text{H}\alpha$) is similar to that of the Galactic extinction curve (or other common curves for that matter), a result that could have been anticipated from the fact that the Balmer line ratios alone can be well fit with the Galactic extinction curve (e.g., Figure 6). It is for this reason that $E(B - V)_{\text{neb}}^{\text{eff}} \simeq E(B - V)_{\text{neb}}^{\text{B}}$, since both are determined at wavelengths proximate to the Balmer lines where the shapes of the individual nebular attenuation curves are not substantially different from that of the Galactic extinction curve. The deviation in the shape of the nebular attenuation curve from other standard curves only becomes apparent when consid-

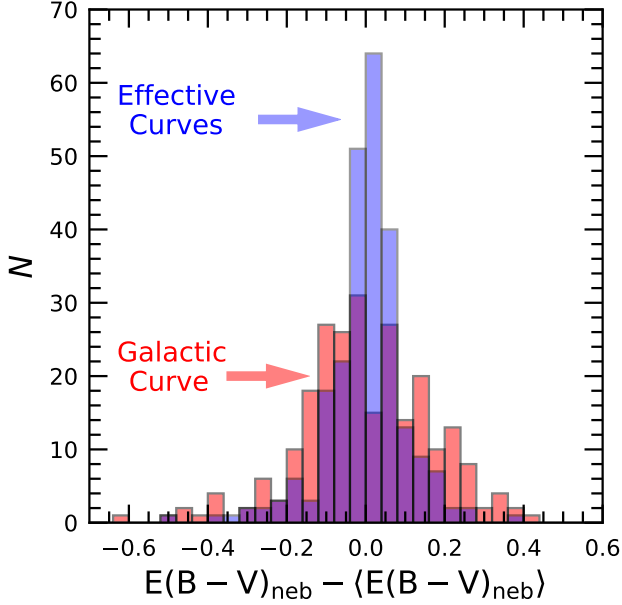


Figure 9. Difference in the reddening computed using multiple line ratios and the average reddening for individual galaxies, shown for all 24 galaxies in the sample, assuming the individual effective nebular attenuation curves (blue histogram) and the Galactic extinction curve (red histogram).

ering the Balmer and Paschen lines together, a point that is discussed further in Section 5.4.

The reliability of the individual effective nebular attenuation curves can be assessed by determining the consistency of the reddening values derived from different line ratios for the same galaxy. For each galaxy, multiple estimates of $E(B - V)_{\text{neb}}$ were calculated using each available line ratio relative to $H\alpha$. The differences between these multiple $E(B - V)_{\text{neb}}$ estimates and their average for all 24 galaxies, are shown in Figure 9. The red and blue histograms indicate the distributions of these reddening differences, assuming the Galactic extinction curve and the individual effective nebular attenuation curves, respectively. As expected, the individual effective nebular attenuation curves yield a narrower spread in $E(B - V)_{\text{neb}}$ calculated from multiple line ratios, compared to the Galactic extinction curve. The standard deviation of the reddening differences computed with the individual nebular attenuation curves is $\sigma = 0.10$, compared to $\sigma = 0.17$ for the Galactic extinction curve. The difference in the spread of reddening values derived using independent line ratios implies nebular attenuation curves that are better able to simultaneously reproduce these line ratios relative to the Galactic extinction curve.

The average nebular dust attenuation curve, $\langle k'(\lambda) \rangle$, was derived by simply averaging the $k'(\lambda)$ of the 24 galaxies, and is shown in Figure 10. The uncertainty in $\langle k'(\lambda) \rangle$ includes both measurement errors and sample variance. The fifth-order polynomial fit to $\langle k'_{\text{neb}}(\lambda) \rangle$ derived for the 24 galaxies

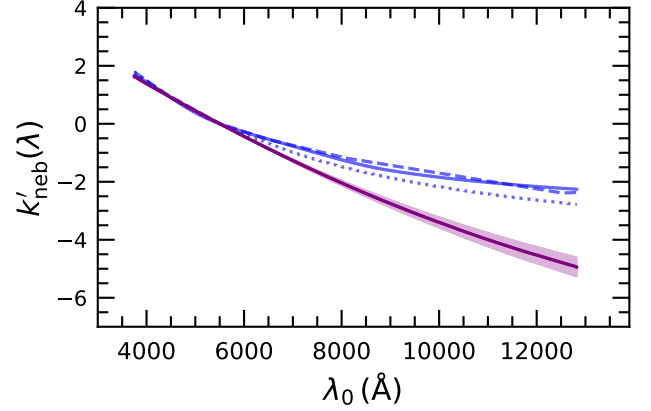


Figure 10. The average $k'_{\text{neb}}(\lambda)$ curve and its 1σ confidence interval are indicated by the solid purple and light shaded regions, respectively. The curves expected for the Galactic, SMC, and Calzetti curves are shown by the solid, dotted, and dashed blue lines, respectively.

is as follows:

$$\langle k'_{\text{neb}}(\lambda) \rangle = -14.198 + \frac{17.002}{\lambda/\mu\text{m}} - \frac{8.086}{(\lambda/\mu\text{m})^2} + \frac{2.177}{(\lambda/\mu\text{m})^3} - \frac{0.319}{(\lambda/\mu\text{m})^4} + \frac{0.021}{(\lambda/\mu\text{m})^5}, \quad (11)$$

valid over the range $0.35 \lesssim \lambda \lesssim 1.28 \mu\text{m}$. The average nebular dust attenuation curve has slightly less curvature than that of common extinction and attenuation curves at $\lambda \lesssim 5500 \text{ \AA}$, and exhibits a substantially steeper wavelength dependence than other common curves at near-IR wavelengths, similar to the behavior noted for the individual $k'_{\text{neb}}(\lambda)$ curves shown in Figure 8. Equation 11 can be used to determine the dust-corrected ratio between two nebular lines, as the ratio does not depend on the normalization of the nebular attenuation curve. However, we caution against using this curve at wavelengths far beyond the range used to constrain it. Absolute line fluxes do require some constraint or assumption on the normalization of the nebular attenuation curve, a point that is discussed further in Section 4.4.

4.3. Applicability to Higher-Redshift Galaxies

Though we have computed $\langle k'_{\text{neb}}(\lambda) \rangle$ for a subset of 24 galaxies in the AURORA sample, we can examine whether the line ratios for galaxies with line coverage insufficient to make it into the final sample are consistent with the average nebular attenuation curve. There are 9 additional galaxies with coverage of at least 3 Balmer lines, 5 of which have redshifts $z > 3$, for which we were able to derive stringent constraints on $k'_{\text{neb}}(\lambda)$. The $k'_{\text{neb}}(\lambda)$ for the 9 galaxies are shown in Figure 11, along with the average nebular attenuation curve calculated using the main sample of 24 galaxies. The individual $k'_{\text{neb}}(\lambda)$ for the 9 additional galaxies, and in particular those at $z > 3$, scatter around the average curve, suggesting no significant redshift evolution in the shape of

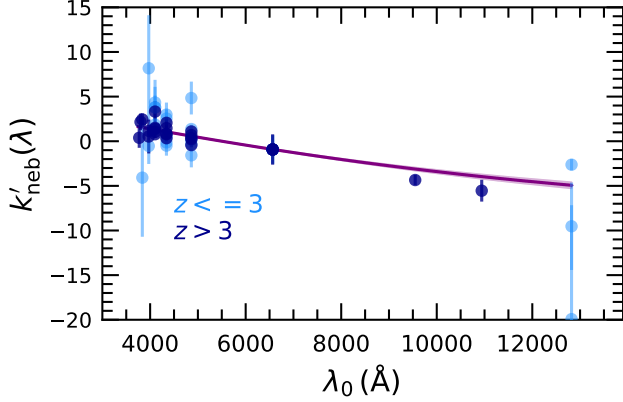


Figure 11. $k'_{\text{neb}}(\lambda)$ versus λ_0 for 4 and 5 galaxies at $z \leq 3$ (light blue symbols) and $z > 3$ (dark blue symbols), respectively, compared with the average curve found for the 24 galaxies in the main sample (purple curve).

the curve. Thus, our results tentatively suggest that the average curve may be applied over a broad range of redshifts. Larger samples of galaxies at $z \gtrsim 3$ with multiple detections of Balmer lines and detections of higher-order Paschen lines (e.g., Pa6 and higher; Figure 3) will be needed to robustly test for any possible redshift evolution in the shape of the nebular attenuation curve, particularly when restricting such samples to similar ranges of SFR, mass, metallicity, and other properties known to correlate with dust attenuation.

4.4. Normalization of the Nebular Dust Attenuation Curve

The $k'_{\text{neb}}(\lambda)$ presented above is arbitrarily normalized such that $k'_{\text{neb}}(V) = 0$ (Section 4.1). Thus $k_{\text{neb}}(\lambda)$ at V band, i.e., $k_{\text{neb}}(V)$, is simply equivalent to R_V , the ratio of the total to selective extinction; i.e., R_V is directly related to the normalization of the dust attenuation curve (Equation 10). Translating the relative attenuation curve to a total effective attenuation curve is typically accomplished by either extrapolating the relative curve to some sufficiently long wavelength and forcing the total attenuation to be zero at this wavelength (e.g., Calzetti 1997; Battisti et al. 2017; Reddy et al. 2015, 2020); or, in the case of a stellar reddening curve, assuming that the integrated absorbed luminosity is re-radiated at infrared wavelengths and using infrared luminosities to constrain the normalization of the dust curve (Calzetti et al. 2000). In principle, this second method can be adapted to constrain the normalization of the nebular attenuation curve by requiring that the inferred dust-corrected nebular-based SFR agrees with the total bolometric SFR taken as the sum of the unobscured UV-based SFR and the dust-obscured IR-based SFR. If there are reasons to suspect that such SFRs should not agree—as is the case when one adopts an age-independent conversion between luminosity and SFR for a galaxy undergoing a burst of star formation where the H I recombination line flux responds more quickly to changes in SFR than the UV and IR luminosities—then this second method may not be accurate.

For simplicity, in the present analysis, we considered the first method of constraining the normalization of the relative nebular dust attenuation curve. Similar to the behavior of other common extinction and attenuation curves, the nebular attenuation curve is assumed to fall to zero (“zero wavelength”) around $\lambda_0 \simeq 2.8 \mu\text{m}$. In general, there are three primary sources of uncertainty in the normalization of the curve: random error from measurement uncertainties in $k'_{\text{neb}}(\lambda)$, systematic error from the functional form used to extrapolate the curve to long wavelengths, and systematic error from the exact wavelength at which the attenuation is forced to be zero. Below, we consider two functional forms of extrapolating the nebular dust attenuation curve to long wavelength: a quadratic and linear function. In Section 5.3, we also consider a new approach to constrain the normalization of the nebular dust attenuation curve.

We first considered a quadratic extrapolation of the attenuation curve to long wavelengths. Lower-upper (LU) decomposition was used to find the quadratic function of $\mu = 1/\lambda$ whose value and derivative (slope) match those of $k'_{\text{neb}}(\lambda)$ at the longest wavelength H I recombination line measured for each galaxy, and where the quadratic function has a minimum value at $\lambda_0 = 2.8 \mu\text{m}$. This minimum value was subtracted from $k'_{\text{neb}}(\lambda)$ for each galaxy to then arrive at the total attenuation curve, $k_{\text{neb}}(\lambda)$. Likewise, LU decomposition was used to find the linear function of $\mu = 1/\lambda$ whose value and derivative (slope) match those of $k'_{\text{neb}}(\lambda)$ at the longest wavelength H I recombination line measured for each galaxy. The value of this linear function at $\lambda_0 = 2.8 \mu\text{m}$ was subtracted from $k'_{\text{neb}}(\lambda)$ for each galaxy to then arrive at the total attenuation curve, $k_{\text{neb}}(\lambda)$.

For the quadratic extrapolation, the R_V vary between $R_V \simeq 2.3$ to 14.2, with a median value of $R_V = 5.5$ and a median fractional uncertainty of $\sigma(R_V)/R_V = 0.22$. The less freedom offered by a simple linear-function extrapolation in μ results in R_V that are on average $\approx 25\%$ larger than those derived from a quadratic extrapolation, varying in the range $R_V \simeq 2.5 - 19.8$ with a median value of $R_V = 6.8$ and a median fractional uncertainty of $\sigma(R_V)/R_V = 0.24$. In both extrapolations, we find that the median R_V is relatively large compared to the values associated with standard dust extinction and attenuation curves. We return to this point in Section 5.1.

To determine the level of systematic uncertainty in R_V stemming from the choice of the zero wavelength, the R_V values were recalculated so that the attenuation curve falls to zero at $3.4 \mu\text{m}$. In this case, the average and median R_V are approximately 4% larger than the comparable values that assume a zero wavelength of $2.8 \mu\text{m}$. The systematic uncertainty in R_V due to the choice of zero wavelength is appreciably smaller than either the measurement uncertainty or the systematic uncertainty arising from the function used to extrapolate the curve to long wavelengths.

5. DISCUSSION

A key result of this analysis is the finding of a relatively high median R_V and a large spread in R_V (Section 4.4)

compared to standard extinction and attenuation curves, including the Galactic, SMC, and Calzetti curves. Section 5.1 summarizes the relationship between R_V and the slope and normalization of the dust attenuation curve, and the R_V that are typically associated with changes in dust grain composition and geometry. Section 5.2 presents a model that encapsulates geometrical variations in the dust distribution by the dust covering fraction. The final normalization of the nebular dust attenuation curves and total nebular attenuation curve are presented in Section 5.3. A comparison of the attenuation curve found in this analysis and that of Reddy et al. (2020) is discussed in Section 5.4. Finally, Section 5.5 presents the physical interpretation of the normalization of the dust curve.

5.1. Dependence of R_V on Dust Grain Composition and Geometry

The total-to-selective extinction ratio, R_V , is related to the optical “slope” of the nebular attenuation curve, commonly defined as $A_{\text{neb}}(B)/A_{\text{neb}}(V)$, by the following equation:

$$\frac{A_{\text{neb}}(B)}{A_{\text{neb}}(V)} = \frac{1}{R_V} + 1. \quad (12)$$

The optical slope can also be expressed as k_B/k_V . By definition, $k_B - k_V \equiv 1$. However, the ratio, k_B/k_V , can be arbitrarily large, with a minimum value of approximately unity for an almost flat attenuation curve where $R_V \rightarrow \infty$.³ Rearranging Equation 12 and combining with Equation 5 yields:

$$R_V = \frac{A_{\text{neb}}(V)}{A_{\text{neb}}(B) - A_{\text{neb}}(V)} = \frac{E(B - V)_{\text{neb}} k'_{\text{neb}}(V)}{A_{\text{neb}}(B) - A_{\text{neb}}(V)}. \quad (13)$$

Since $E(B - V)_{\text{neb}} = A_{\text{neb}}(B) - A_{\text{neb}}(V)$, the above equation reduces to

$$R_V = k_{\text{neb}}(V) = k'_{\text{neb}}(V) + C, \quad (14)$$

where C is the constant of normalization that relates $k'_{\text{neb}}(\lambda)$ and $k_{\text{neb}}(\lambda)$. Since $k'_{\text{neb}}(V) \equiv 0$ (Equation 10), the above equation simply says that R_V is a constant providing the offset between $k'_{\text{neb}}(\lambda)$ and $k_{\text{neb}}(\lambda)$. Thus, R_V is related to both the slope and normalization of the nebular attenuation curve, and is equivalent to the value of the total nebular attenuation curve at V -band. As the normalization of the nebular attenuation curve increases, R_V increases, and the optical slope of the curve becomes shallower.

In the context of line-of-sight *extinction* curves, variations in R_V have been linked to differences in the dust grain size distribution (Fitzpatrick 1999; Draine 2003; Li et al. 2021). Environments where small dust grains are more abundant—such as those affected by supernovae shocks, which thermally sputter large grains, or regions experiencing grain shattering in the warm ionized ISM (e.g., Hirashita et al. 2010)—typically exhibit steeper extinction curves. Such curves result

in more substantial extinction at UV and optical wavelengths, leading to a lower R_V . Conversely, environments that favor the growth of large dust grains—such as through the coagulation of smaller grains in the ISM (e.g., Hirashita 2012; Galliano et al. 2018)—tend to produce flatter, or “grayer,” extinction curves, corresponding to higher R_V . The balance between dust destruction and grain growth determines the overall grain-size distribution and, by extension, the slope and normalization of the extinction curve. The composition of the grains (silicates versus graphitic) may also affect the shape of the extinction curve (Li et al. 2021). Observed sightlines in the Milky Way as well as towards the SMC and LMC exhibit varying extinction curves with R_V values ranging from 2.7 to 5.5 (e.g., Cardelli et al. 1989; Fitzpatrick 1999; Clayton et al. 2000; Gordon et al. 2003; Fitzpatrick & Massa 2009).

In the case of *attenuation* curves, where scattering of light into the line of sight, nonuniform column density distributions, or spatial variations in optical depth are significant, the value of R_V can be arbitrarily large (Narayanan et al. 2018; Trayford et al. 2020). The median R_V values inferred for the AURORA sample range from $\simeq 5.5$ to 6.8 depending on whether a quadratic or linear extrapolation to long wavelength is used (Section 4.4), with some galaxies exhibiting $R_V \gtrsim 10$. These values are notably higher than those typically observed along Galactic sightlines, which usually have $R_V \lesssim 5.5$ across a variety of environments, as illustrated in Figure 12. Consequently, the large R_V inferred for the nebular attenuation curves suggest that their variation is driven primarily by the geometry of the dust relative to the OB associations, rather than by differences in the dust grain size distribution. Specifically, the light from OB associations along low dust-column-density (and thus relatively unobscured) sightlines reduces the effective nebular attenuation at short wavelengths. This leads to a flattening of the attenuation curve and, consequently, a larger R_V .

While we cannot definitely rule out the possibility that some of the variation in the nebular dust attenuation curves is due to differences in dust grain composition or size distribution, there are several pieces of evidence that support a scenario of a non-uniform dust distribution towards OB associations. First, the very high $R_V \gtrsim 5$ values found for most galaxies in the sample relative to the values found along different environments in the Milky Way (Figure 12) suggest the importance of the dust-stars geometry. Second, prior evidence of non-unity gas and metal covering fractions in similar galaxies from other studies (e.g., Shapley et al. 2003; Heckman et al. 2011; Berry et al. 2012; Jones et al. 2013; Alexandroff et al. 2015; Trainor et al. 2015; Henry et al. 2015; Vasei et al. 2016; Reddy et al. 2016b; Steidel et al. 2018; Du et al. 2018; Gazagnes et al. 2018; Trainor et al. 2019; Jaskot & Ravindranath 2016; Harikane et al. 2020; Reddy et al. 2022, among many others) imply a non-unity covering fraction of dust as well. Third, the near-ubiquitous presence of very massive O-star P-Cygni photospheric lines (e.g., C IV $\lambda\lambda 1548, 1550$ for $\gtrsim 30 M_\odot$ O stars and Si IV $\lambda\lambda 1393, 1402$ in O supergiants) and Wolf Rayet features (e.g., He II $\lambda 1640$) in the far-UV spectra of

³ Since $k_B - k_V \equiv 1$, $k_B/k_V \approx 1$ implies that $k_B \gg 1$ and $k_V \gg 1$, and $R_V \gg 1$.

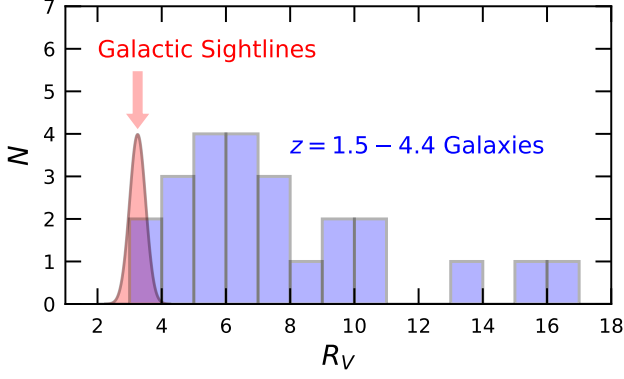


Figure 12. Histogram of R_V for the 24 galaxies in the sample (shown in blue). These effective R_V values were obtained using the methodology explained in Section 5.3. For comparison, the arbitrarily normalized distribution of R_V derived by Zhang et al. (2023) for 3 million stars from the Large Sky Area Multi-Object Fiber Spectroscopy Telescope (LAMOST) survey is shown in red. These authors find a Gaussian distribution of R_V with a mean of 3.25 and standard deviation of 0.25.

high-redshift star-forming galaxies (e.g., Pettini et al. 2000; Shapley et al. 2003) implies that some fraction of even the youngest OB associations must lie along relatively unobscured sightlines. Fourth, spatial offsets between UV and dust emission (e.g., Willott et al. 2015; Pentericci et al. 2016; Schouws et al. 2022; Bowler et al. 2022; Inami et al. 2022) imply some fraction of the OB associations are in dust-free regions. Fifth, differences in the reddening of Balmer and Paschen lines from integrated line measurements (e.g., Reddy et al. 2023b) and, most recently, spatial offsets between $H\alpha$ and Paschen emission (Lorenz et al. 2025) support a scenario of non-uniform dust distribution towards OB associations.

5.2. Modeling with a Sub-unity Covering Fraction of Dust

The high R_V inferred for the sample, and the association of such high values to variations in the dust-stars geometry (e.g., Narayanan et al. 2018; Trayford et al. 2020), suggest that a uniform foreground screen (i.e., with a 100% covering fraction of dust) may not be an appropriate description for at least half the galaxies in the sample. In Section 3, we suggested that differences in the reddenings derived from the Balmer and Paschen lines may indicate the presence of regions with high dust column densities, causing the shorter-wavelength recombination lines which are more heavily attenuated by dust to be dominated by emission from the unreddened regions of the galaxy (see also Reddy et al. 2023b). Along these lines, Lorenz et al. (2025) use JWST/NIRCam medium-band photometry to construct spatially-resolved $H\alpha$ and $\text{Pa}\beta$ maps for a sample of 14 star-forming galaxies at $1.3 \leq z \leq 2.4$. They find that $\lesssim 0''.1$ offsets between $H\alpha$ and $\text{Pa}\beta$ emission are common, suggesting the presence of optically thick star formation. The implied non-uniform distribution of dust along the sightlines to OB

associations in galaxies has been invoked to explain other findings, including the offset between the reddening of the nebular regions and stellar continuum in high-redshift galaxies (Reddy et al. 2020; Lorenz et al. 2023, 2024), and may also account for much of the scatter between dust attenuation, as quantified by the ratio of the infrared-to-UV luminosity, and UV spectral slope (i.e., the IRX- β diagram; Burgarella et al. 2005; Reddy et al. 2006; Bouwens et al. 2016; Buat et al. 2018; Reddy et al. 2018a; Salim & Boquien 2019; see also review by Salim & Narayanan 2020). In principle, the Calzetti curve includes the effects of a non-unity covering fraction of dust on the attenuation of the stellar continuum of nearby starburst galaxies (Calzetti et al. 2000), but even this curve is unable to reconcile the full suite of Balmer and Paschen emission-line ratios accessible in this study for a majority of galaxies in the present sample. The primary distinction here, of course, is that we are concerned with the distribution of dust along the sightlines to the H II regions around massive stars, since that is where the recombination lines originate, rather than the distribution of dust towards the stars dominating the (non-ionizing) stellar continuum. Here, we discuss a model of the attenuation that allows for a non-uniform distribution of dust.

5.2.1. Formalism

Variations in dust optical depth within a galaxy can be parameterized by introducing another factor in addition to the reddening, namely the dust covering fraction, f_{cov} . In this section, we build upon the simple foreground screen model expressed in Equation 1 to account for a non-unity covering fraction of dust, akin to the formalism used to model the rest-frame UV continuum light of galaxies with a non-unity covering fraction of gas and dust (e.g., Reddy et al. 2016a,b; Steidel et al. 2018; see also Förster Schreiber et al. 2001; Prescott et al. 2022). We assume a simple model (referred to as the “covering-fraction model”) in which some fraction of the intrinsic line emission escapes unimpeded, while the remaining fraction is subject to dust reddening, as shown in the schematic diagram of Figure 13. We define the uncovered, or unreddened, emission as

$$f_{\text{unred}}(\lambda) = (1 - f_{\text{cov}})f_0(\lambda) \quad (15)$$

and the covered, or reddened, emission as

$$f_{\text{red}}(\lambda) = f_{\text{cov}}f_0(\lambda) \times 10^{-0.4E(B-V)_{\text{neb}}^{\text{cov}}k_{\text{neb}}(\lambda)}, \quad (16)$$

where f_{cov} denotes the covering fraction of dust, and $E(B - V)_{\text{neb}}^{\text{cov}}$ is the reddening of the dust-covered portion of the line emission. In this case, the sum of the unreddened and reddened line emission constitutes the observed line flux:

$$\begin{aligned} f(\lambda) &= f_{\text{unred}}(\lambda) + f_{\text{red}}(\lambda) \\ &= (1 - f_{\text{cov}})f_0(\lambda) + \\ &\quad f_{\text{cov}}f_0(\lambda) \times 10^{-0.4E(B-V)_{\text{neb}}^{\text{cov}}k_{\text{neb}}(\lambda)}. \end{aligned} \quad (17)$$

The first and second terms of this equation correspond to the unreddened and reddened components, respectively. In this

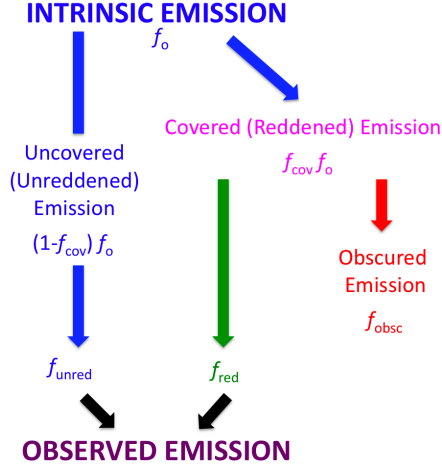


Figure 13. Schematic diagram of the covering-fraction model. Some fraction of the H I line emission escapes the galaxy unimpeded by dust, denoted as the uncovered (unreddened) emission (blue). The remaining fraction is reddened by dust (covered reddened emission), some of which exits the galaxy (green) and some of which is absorbed by dust and reemitted in the infrared (obscured emission, red). The uncovered and reddened emission both contribute to the total observed H I line emission.

model, a fixed fraction of the *intrinsic* flux is subject to reddening (f_{cov}) or escapes unimpeded ($1 - f_{\text{cov}}$), independent of wavelength. The actual *fraction* of the intrinsic flux extinguished by dust (i.e., the ratio of the “obscured emission” to the intrinsic emission as depicted in Figure 13) is, of course, wavelength dependent, and is given by

$$\begin{aligned} \mathcal{F}_{\text{obsc}}(\lambda) &= \frac{f_{\text{obsc}}(\lambda)}{f_0(\lambda)} \\ &= \frac{f_{\text{cov}} f_0(\lambda) [1 - 10^{-0.4E(B-V)_{\text{neb}}^{\text{cov}} k_{\text{neb}}(\lambda)}]}{f_0(\lambda)} \\ &= f_{\text{cov}} [1 - 10^{-0.4E(B-V)_{\text{neb}}^{\text{cov}} k_{\text{neb}}(\lambda)}]. \end{aligned} \quad (18)$$

The fraction of the *observed* line emission that emerges from the unreddened regions is also wavelength dependent. For a given combination of f_{cov} and $E(B - V)_{\text{neb}}^{\text{cov}}$, the fraction of light emerging from the unreddened regions, $\mathcal{F}_{\text{unred}}(\lambda)$ —defined as the ratio of the uncovered (unreddened) emission to the total observed emission, referring again to Figure 13—decreases with increasing wavelength. Mathematically,

$$\begin{aligned} \mathcal{F}_{\text{unred}}(\lambda) &= \frac{f_{\text{unred}}(\lambda)}{f(\lambda)} \\ &= \frac{f_{\text{unred}}(\lambda)}{f_{\text{unred}}(\lambda) + f_{\text{red}}(\lambda)} \\ &= \frac{1 - f_{\text{cov}}}{1 - f_{\text{cov}} + f_{\text{cov}} \times 10^{-0.4E(B-V)_{\text{neb}}^{\text{cov}} k_{\text{neb}}(\lambda)}} \end{aligned} \quad (19)$$

These fractions are shown as a function of wavelength in Figure 14, for two different combinations of f_{cov} and $E(B -$

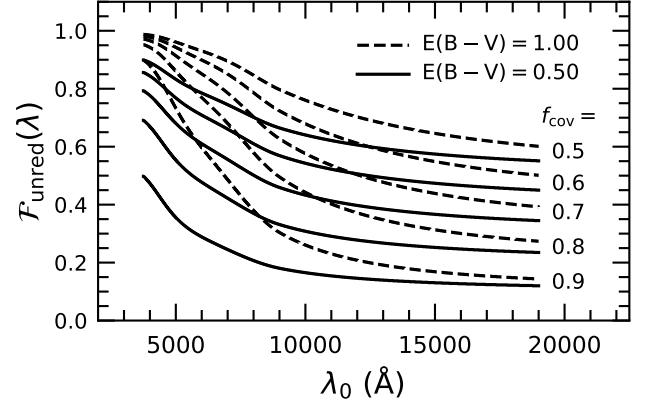


Figure 14. The fraction of observed line emission coming from the unobscured regions as a function of wavelength assuming a subunity covering fraction of dust and the Galactic extinction curve, as described by Equation 17. The solid and dashed curves correspond to $E(B - V)_{\text{neb}}^{\text{cov}} = 0.50$ and 1.00 respectively, for the different values of f_{cov} indicated in the figure. For a fixed covering fraction of dust, a smaller fraction of the observed emission arises from the unreddened regions for the longer-wavelength Paschen lines relative to the shorter-wavelength Balmer lines.

$V)_{\text{neb}}^{\text{cov}}$ assuming a “line-of-sight” extinction given by the Galactic extinction curve. For example, for $f_{\text{cov}} = 0.70$ and $E(B - V)_{\text{neb}}^{\text{cov}} = 0.50$, the fraction of the observed H α emission emerging from low-dust-optical-depth (i.e., unreddened) regions is $\mathcal{F}_{\text{unred}} = 0.58$. For the same conditions, $\mathcal{F}_{\text{unred}} = 0.39$ at the wavelength of Pa5; i.e., a larger fraction of the observed Pa5 flux comes from the reddened regions compared to H α . For the same f_{cov} and $E(B - V)_{\text{neb}}^{\text{cov}} = 1.00$, the unreddened percentage increases to 82% for H α and 48% for Pa5; i.e., at a fixed f_{cov} , an increase in $E(B - V)_{\text{neb}}^{\text{cov}}$ leads to a decrease in the fraction of observed flux coming from the reddened regions and an increase in the fraction from unreddened regions, for any given emission line.

It is important to emphasize that $\mathcal{F}_{\text{unred}}(\lambda)$ represents the fraction of the *observed*, rather than the *intrinsic*, light that is unimpeded by dust. Accordingly, $\mathcal{F}_{\text{unred}}(\lambda)$ may be large under two conditions: (a) when the covering fraction is small (for $f_{\text{cov}} = 0$, $\mathcal{F}_{\text{unred}} = 1$ at all wavelengths), or (b) when $E(B - V)_{\text{neb}}^{\text{cov}}$ is large. In the latter case, the fraction of the observed line emission from regions with high $E(B - V)_{\text{neb}}^{\text{cov}}$ —i.e., the optically-thick regions—decreases, leading to a higher value of $\mathcal{F}_{\text{unred}}(\lambda)$ at a given f_{cov} . If $E(B - V)_{\text{neb}}^{\text{cov}}$ is extremely large (i.e., $E(B - V)_{\text{neb}}^{\text{cov}} \gg 1$) such that even the Paschen lines become optically-thick, then $\mathcal{F}_{\text{unred}}$ will be uniformly high for all the Balmer and Paschen lines. In such a scenario, mid- or far-IR line and/or dust continuum measurements may be needed to determine whether the covering fraction is high or low.

5.2.2. Distribution of $E(B - V)_{\text{neb}}^{\text{cov}}$ and f_{cov}

In the covering-fraction model, R —as defined in Equation 3—can be expressed as follows:

$$R = \log_{10} \left[\frac{1 - f_{\text{cov}} + f_{\text{cov}} \times 10^{-0.4E(B-V)_{\text{neb}}^{\text{cov}} k_{\text{neb}}(\lambda_1)}}{1 - f_{\text{cov}} + f_{\text{cov}} \times 10^{-0.4E(B-V)_{\text{neb}}^{\text{cov}} k_{\text{neb}}(\lambda_2)}} \right]. \quad (20)$$

Again, $H\alpha$ is used as the reference line. Fitting the R measured for each galaxy using Equation 20 yields an estimate of the best-fit f_{cov} and $E(B-V)_{\text{neb}}^{\text{cov}}$. The covering-fraction model fits with the Galactic extinction curve for k_{neb} are shown in Figure 15 for two galaxies in the sample having $E(B-V)_{\text{neb}}^{\text{B}} < E(B-V)_{\text{neb}}^{\text{P}}$. While the Galactic extinction curve with $f_{\text{cov}} = 1$ is not able to simultaneously predict all the Balmer and Paschen line ratios (Section 3), a model with $f_{\text{cov}} < 1$ is able to reproduce all the line ratios for these two galaxies and, in general, the full sample of 24 galaxies. Adopting an SMC or Calzetti curve for k_{neb} results in $E(B-V)_{\text{neb}}^{\text{cov}}$ that are on average 0.02 mag redder and 0.13 mag bluer, respectively, than those obtained with the Galactic extinction curve. Likewise, relative to the covering fractions derived with the Galactic extinction curve, $\delta f_{\text{cov}} = 0.03$ smaller and 0.03 larger, respectively, for the SMC and Calzetti curves. Regardless of the adopted extinction or attenuation curve, the covering-fraction model provides improved fits for R versus λ_0 relative to the model which assumes a unity covering fraction.

The distribution of f_{cov} and $E(B-V)_{\text{neb}}^{\text{cov}}$ for the full sample is displayed in Figure 16. Covering fractions vary from $\simeq 0.50$ to unity. Note that there are marginal anticorrelations between the random uncertainties in f_{cov} and $E(B-V)_{\text{neb}}^{\text{cov}}$ on the one hand, and f_{cov} on the other; i.e., the random uncertainties in f_{cov} and $E(B-V)_{\text{neb}}^{\text{cov}}$ are on average larger at lower f_{cov} . The larger uncertainties for these galaxies may be due to lower S/N in the lines, fewer number of lines, or a smaller wavelength baseline of the lines being fit, which may indicate that the covering-fraction modeling prefers lower f_{cov} for such galaxies. In Appendix B, we present a discussion of these possibilities, and the results of a simulation to test for biases in the derived f_{cov} and $E(B-V)_{\text{neb}}^{\text{cov}}$. From this analysis, we conclude that the larger uncertainties for galaxies with lower f_{cov} is primarily due to lower S/N in the lines being fit, and that there is no biasing effect that would cause such galaxies to be preferentially fit with lower f_{cov} .

The improved fits to R provided by the covering-fraction model are perhaps not surprising, given that this model introduces a second free parameter—the covering fraction. However, it offers a more accurate representation of a non-uniform distribution of dust, which has been suggested by previous studies, and is also supported by the high R_V inferred for the nebular dust attenuation curves (Section 4.4).

5.2.3. Light-weighted Reddening

For the covering-fraction model, the fraction of the observed line luminosity that emerges from the unreddened regions of a galaxy is wavelength dependent, as noted earlier (Figure 14). Thus, the reddening that one measures for a galaxy will depend on the wavelength of the lines used to

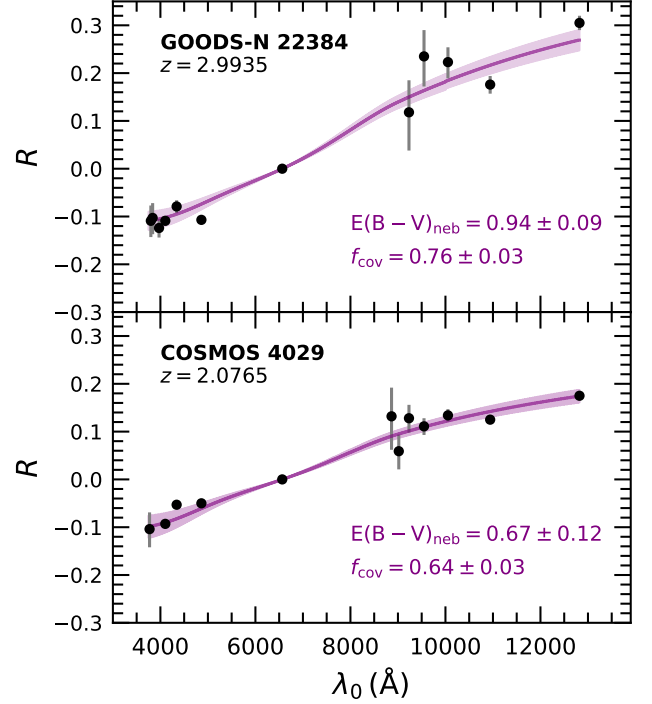


Figure 15. R versus rest-frame wavelength for two galaxies in the sample. The measured values and uncertainties in R are indicated by the black points and errorbars. The solid lines and shaded regions indicate the best-fit models that incorporate a sub-unity covering fraction of dust and 68% confidence intervals of those fits, respectively. The best-fit values of f_{cov} and $E(B-V)_{\text{neb}}^{\text{cov}}$ for the Galactic extinction curve are indicated in each panel.

measure the reddening: i.e., the light-weighted reddening, $E(B-V)_{\text{neb}}^{\text{lw}}$, also varies with wavelength. Specifically, the reddening computed from the (shorter wavelength) Balmer lines alone will be weighted more heavily towards the unreddened sightlines, while the reddening computed from the (longer wavelength) Paschen lines alone will be weighted towards the reddened sightlines. This variation naturally occurs because the shorter wavelength lines are more heavily attenuated by dust than the longer wavelength lines for a given dust column density (or reddening). The consistency of the covering-fraction model can be checked by comparing the light-weighted reddening at a given wavelength to the reddening deduced using only the recombination lines spanning a similar wavelength range. Any discrepancies between the two can provide insight into the accuracy of the model assumptions and the distribution of dust and stars in the galaxy.

The light-weighted reddening, $E(B-V)_{\text{neb}}^{\text{lw}}$, can be expressed as the product of two factors: the reddening of the covered portion of light ($E(B-V)_{\text{neb}}^{\text{cov}}$) and the fraction of the observed line luminosity that is reddened, $\mathcal{F}_{\text{red}}(\lambda) = 1 - \mathcal{F}_{\text{unred}}(\lambda)$, which can be obtained from Equation 19, i.e.,

$$\begin{aligned} E(B-V)_{\text{neb}}^{\text{lw}} &= E(B-V)_{\text{neb}}^{\text{cov}} \times \mathcal{F}_{\text{red}}(\lambda) \\ &= E(B-V)_{\text{neb}}^{\text{cov}} \times \end{aligned}$$

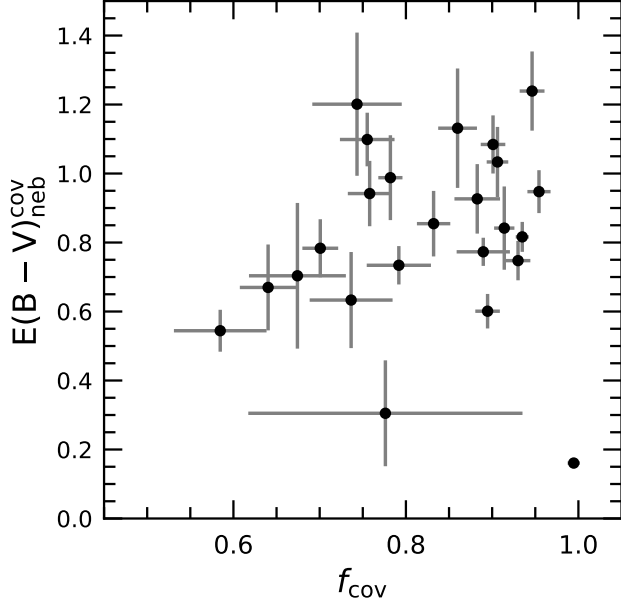


Figure 16. Distribution of f_{cov} and $E(B-V)_{\text{neb}}^{\text{cov}}$ for the full sample of galaxies, derived from the model with a sub-unity dust covering fraction.

$$\left[\frac{f_{\text{cov}} \times 10^{-0.4E(B-V)_{\text{neb}}^{\text{cov}} k_{\text{neb}}(\lambda)}}{1 - f_{\text{cov}} + f_{\text{cov}} \times 10^{-0.4E(B-V)_{\text{neb}}^{\text{cov}} k_{\text{neb}}(\lambda)}} \right] \quad (21)$$

Since \mathcal{F}_{red} is larger at longer wavelengths for a given f_{cov} and $E(B-V)_{\text{neb}}^{\text{cov}}$ (see Figure 14), the reddening measured at these wavelengths will be weighted more heavily towards the reddened regions, leading to a higher value of the light-weighted reddening, $E(B-V)_{\text{neb}}^{\text{lw}}$, in comparison to the shorter-wavelength Balmer lines.

The light-weighted reddening as a function of wavelength for two galaxies in the sample (GOODSN-22384 and COSMOS-4029) is shown in Figure 17. For comparison, $E(B-V)_{\text{neb}}^{\text{B}}$, $E(B-V)_{\text{neb}}^{\text{P}}$, and their associated uncertainties are also shown in this figure. For these two galaxies, $E(B-V)_{\text{neb}}^{\text{lw}}$ averaged over the wavelength ranges of the Balmer and Paschen lines is similar to the reddening computed from either the Balmer lines alone, or the Paschen lines alone, assuming a uniform screen of dust. More generally, we find that the covering-fraction model predicts light-weighted reddenings that are consistent with those deduced from either the Balmer or Paschen lines for most galaxies in the sample.

To illustrate this, Figure 18 compares $E(B-V)_{\text{neb}}^{\text{lw}}$ calculated from the covering-fraction modeling with the $E(B-V)_{\text{neb}}$ computed from either the Balmer (blue points) or Paschen lines (red points) assuming unity covering fraction of dust for the full sample of galaxies. The light-weighted reddening is computed at 5400 and 9500 Å, roughly corresponding to the mean wavelengths of the Balmer and Paschen lines, respectively, available for most galaxies. As noted in Section 3, the Balmer lines provide more constraining power on $E(B-V)_{\text{neb}}$ because of their sensitivity to the reddening

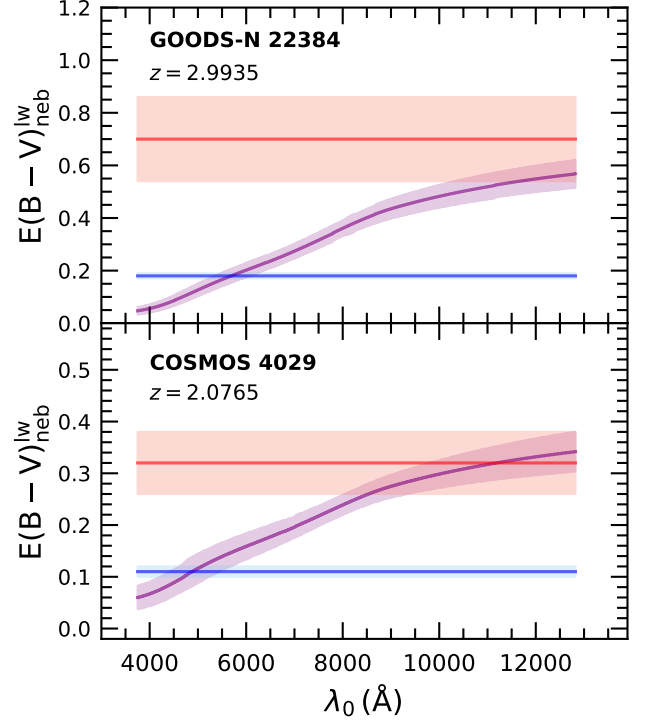


Figure 17. Light-weighted reddening, $E(B-V)_{\text{neb}}^{\text{lw}}$, and its 1σ confidence interval as a function of wavelength (purple curve and shaded regions, respectively) for GOODSN-22384 (top panel) and COSMOS-4029 (bottom panel). For comparison, $E(B-V)_{\text{neb}}^{\text{B,P}}$ and their 1σ uncertainties are indicated by the horizontal blue and red lines and shaded regions, respectively.

and their typically higher S/N than the Paschen lines. For the tightly constrained reddening deduced from the Balmer lines alone, we find that the covering-fraction model successfully predicts $E(B-V)_{\text{neb}}^{\text{B}}$ for all but one of the galaxies in the sample. This one exception is COSMOS-4622, where $E(B-V)_{\text{neb}}^{\text{lw}} = 0.542 \pm 0.075$ computed at ~ 5400 Å, while $E(B-V)_{\text{neb}}^{\text{B}} = 0.769 \pm 0.018$. This discrepancy is due to the fact that the line ratios for this particular galaxy are not as well fit by the covering-fraction model, as evidenced by a somewhat lower χ^2 value for the fit relative to the χ^2 values for most other galaxies in the sample.

The most notable outliers in the comparison of the light-weighted reddening at 9500 Å and the Paschen-derived reddening are the same four galaxies mentioned in Section 3 for which the Paschen-derived reddening is negligible. Aside from these outliers, the covering-fraction model successfully reproduces the reddening computed from either the Balmer or Paschen lines for the vast majority of galaxies in the sample.

5.3. Normalization Constraints from the Covering-Fraction Modeling and the Total Nebular Attenuation Curve

An alternative method of constraining the normalization of the effective attenuation curve is to require that intrinsic

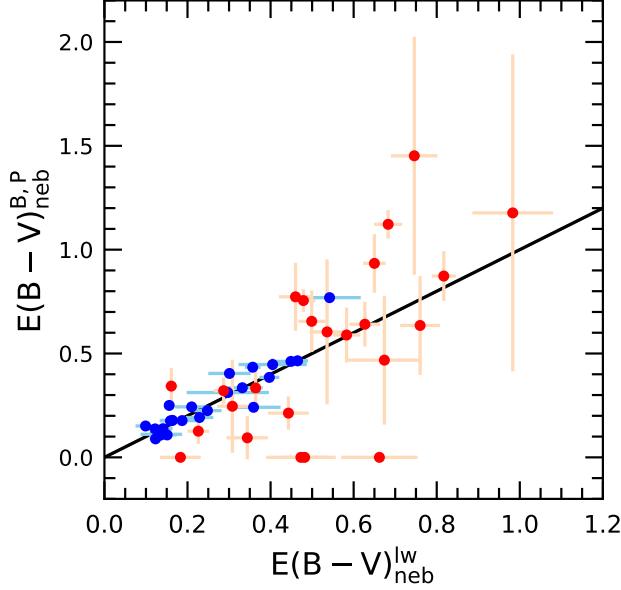


Figure 18. Comparison of the light-weighted reddening from the covering-fraction model computed at 5400 and 9500 Å with $E(B - V)_{\text{neb}}^{\text{B,P}}$ (blue points) and $E(B - V)_{\text{neb}}^{\text{P}}$ (red points). The line of equality is indicated in black.

line fluxes derived using this curve match those predicted by the covering-fraction model (Section 5.2). Using Equation 17, intrinsic H I emission line fluxes were calculated for each galaxy based on the $E(B - V)_{\text{neb}}^{\text{cov}}$ and f_{cov} presented in Section 5.2. These intrinsic line fluxes, along with the observed line fluxes, were used to calculate the normalization of $k'_{\text{neb}}(\lambda)$. The “effective” R_V computed in this manner vary in the range $R_V^{\text{eff}} \simeq 3.2 - 16.4$, and typically lie between the R_V computed using the quadratic and linear long-wavelength extrapolations of the attenuation curve.

Using the constraints on the intrinsic line fluxes from the covering-fraction model, we find a median $R_V^{\text{eff}} = 6.957$ for the 24 galaxies. Combining this with the relative attenuation curve (Equation 11), we obtain the following for the total (average) nebular attenuation curve:

$$\langle k_{\text{neb}}(\lambda) \rangle = -7.241 + \frac{17.002}{\lambda/\mu\text{m}} - \frac{8.086}{(\lambda/\mu\text{m})^2} + \frac{2.177}{(\lambda/\mu\text{m})^3} - \frac{0.319}{(\lambda/\mu\text{m})^4} + \frac{0.021}{(\lambda/\mu\text{m})^5}, \quad (22)$$

again valid over the wavelength range $0.35 \lesssim \lambda \lesssim 1.28 \mu\text{m}$. The average and individual effective nebular attenuation curves are compared with other common extinction and attenuation curves in Figure 19. As noted before, the average nebular attenuation curve has a shape similar to that of other common extinction and attenuation curves at $\lambda \lesssim 5500 \text{ Å}$. However, the large difference in normalization between the average curve derived for the AURORA sample and the Galactic, SMC, and Calzetti curves becomes apparent only

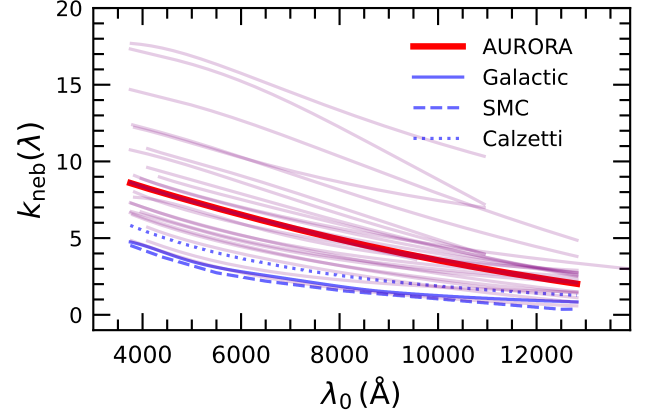


Figure 19. The average nebular attenuation curve, $k_{\text{neb}}(\lambda)$, versus λ_0 for the main sample of 24 galaxies (thick red curve). The individual nebular dust attenuation curves are indicated by the light purple lines. The curves for the Galactic, SMC, and Calzetti curves are shown by the solid, dotted, and dashed blue lines, respectively.

when the Paschen line fluxes are considered jointly with the Balmer line fluxes.

5.4. Comparison to the Reddy et al. (2020) Nebular Attenuation Curve

Reddy et al. (2020) used ground-based optical spectroscopic data from the MOSFIRE Deep Evolution Field (MOSDEF) survey (Kriek et al. 2015) to provide the first constraints on the shape of the nebular attenuation curve at $z \sim 2$. Based on the first five low-order Balmer lines detected in the composite spectrum of 532 star-forming galaxies accessible in that study, they found a nebular attenuation curve that closely resembles other common extinction and attenuation curves, including the Galactic extinction curve of Cardelli et al. (1989), within the uncertainties. As noted in Section 4.2, the average nebular attenuation curve found in this work also has a shape similar to that of the Galactic extinction curve at $\lambda \lesssim 5500 \text{ Å}$, consistent with the shape found by Reddy et al. (2020). The key difference, however, is that this analysis indicates a substantially higher $R_V = 6.96$ than that of the Galactic extinction curve ($R_V \simeq 3.1$), a result that only becomes apparent with the inclusion of longer-wavelength, less-reddening-sensitive near-IR Paschen line measurements made possible by JWST, and which were unavailable for the MOSDEF sample. For most galaxies in the sample, the Paschen-only line ratios, as well as those formed from a combination of Paschen and Balmer lines, suggest the presence of star formation that is optically thick in the Balmer lines, leading to a higher R_V than the Galactic extinction curve.

5.5. Physical Interpretation of the Normalization of the Effective Attenuation Curve

In the covering-fraction model (Section 5.2), the geometry of dust and stars is encapsulated by the covering fraction of

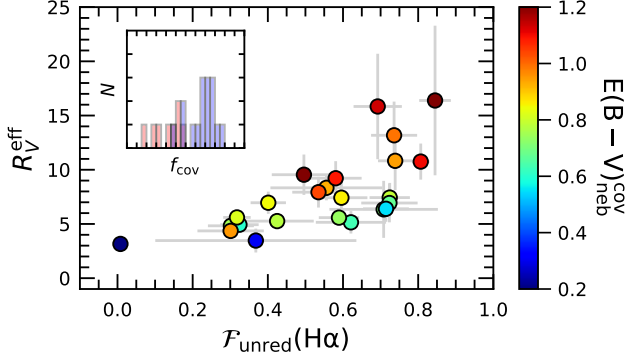


Figure 20. R_V^{eff} as a function of the unreddened fraction of light contributing to the observed $\text{H}\alpha$ line flux, $\mathcal{F}_{\text{unred}}(\text{H}\alpha)$, for the 24 galaxies in the sample. The points are color-coded by $E(B-V)_{\text{neb}}^{\text{cov}}$ as determined from the covering-fraction model. The inset panel shows the histogram of f_{cov} for galaxies with $\mathcal{F}_{\text{unred}}(\text{H}\alpha) > 0.7$ (red) and $\mathcal{F}_{\text{unred}}(\text{H}\alpha) < 0.7$ (blue).

dust (f_{cov}) and reddening ($E(B-V)_{\text{neb}}^{\text{cov}}$), which parameterize the variation in optical depths along the sightlines to OB associations. The unreddened fraction of the observed line flux at a given wavelength predicted by this model (see Section 5.2 and Figure 14) should correlate with R_V , allowing us to connect the normalization of the effective attenuation curve to the physically motivated covering-fraction model. As shown in Figure 20 for the 24 galaxies in the present sample, R_V progressively increases as the fraction of unreddened light contributing to the observed $\text{H}\alpha$ flux rises. From a Spearman test, the probability of a null correlation between R_V and $\mathcal{F}_{\text{unred}}(\text{H}\alpha)$ is $p = 5.6 \times 10^{-5}$, and remains highly significant ($p < 0.0008$) regardless of the method used to constrain R_V . This holds true whether R_V is determined using a quadratic or linear extrapolation, or by forcing the intrinsic line fluxes to match those predicted by the covering-fraction model, as all approaches yield R_V that correlate strongly with each other.

Recall that $\mathcal{F}_{\text{unred}}(\lambda)$ may be elevated either due to a low f_{cov} or a high $E(B-V)_{\text{neb}}^{\text{cov}}$ (see Section 5.2.1). Our analysis suggests that both factors are at play. The inset panel in Figure 20 presents histograms of f_{cov} for galaxies above and below $\mathcal{F}_{\text{unred}}(\text{H}\alpha) = 0.7$. Galaxies with $\mathcal{F}_{\text{unred}}(\text{H}\alpha) > 0.7$ show a systematically lower f_{cov} (with a median $f_{\text{cov}} = 0.72$) compared to galaxies with $\mathcal{F}_{\text{unred}}(\text{H}\alpha) < 0.7$ (with a median $f_{\text{cov}} = 0.90$). Moreover, the color-coding of points in Figure 20 demonstrates that galaxies exhibiting higher $\mathcal{F}_{\text{unred}}(\text{H}\alpha)$ also tend to have systematically redder $E(B-V)_{\text{neb}}^{\text{cov}}$.

The relationship between R_V and $\mathcal{F}_{\text{unred}}(\lambda)$, along with the scatter in this relationship, provides valuable insights into the underlying factors that contribute to variations in R_V within the sample. In particular, the correlation of this scatter with $E(B-V)_{\text{neb}}^{\text{cov}}$ and f_{cov} implies that these two factors are key drivers of the observed variation in R_V . Given the considerable interest in understanding how attenuation

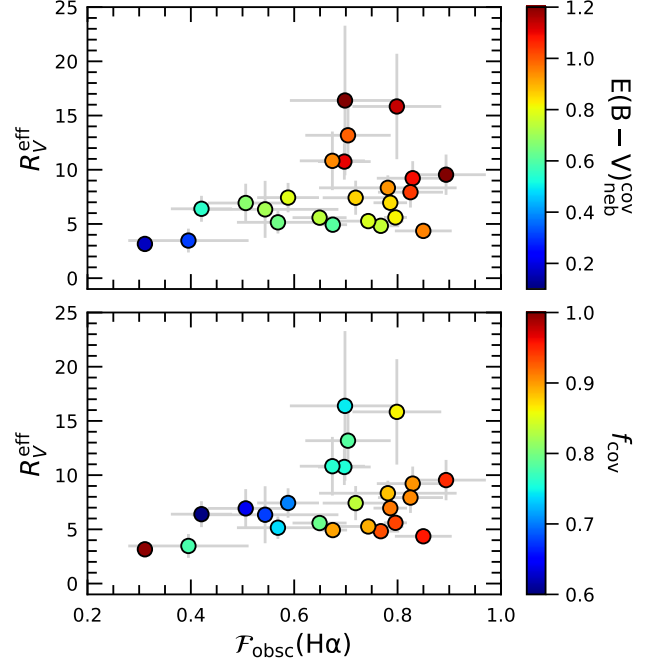


Figure 21. R_V^{eff} as a function of the fraction of dust-obscured $\text{H}\alpha$ luminosity, $\mathcal{F}_{\text{obs}}(\lambda)$, as given in Equation 18. The symbols in the top and bottom panels are color coded by $E(B-V)_{\text{neb}}^{\text{cov}}$ and f_{cov} , respectively, as determined from the covering-fraction model.

curves vary in the dustiest galaxies, we can further investigate how R_V changes with respect to the fraction of intrinsic luminosity that is obscured, i.e., $\mathcal{F}_{\text{obs}}(\lambda)$ (Equation 18), as shown in Figure 21. Galaxies with the highest values of R_V in the sample (e.g., $R_V \gtrsim 10$) tend to be more “dusty,” where a larger fraction of the intrinsic $\text{H}\alpha$ luminosity is obscured by dust. Conversely, the dustiest galaxies in the sample (e.g., those with $\mathcal{F}_{\text{obs}}(\text{H}\alpha) \gtrsim 0.70$) exhibit a range of R_V values that depend on the dust-covering fraction, f_{cov} , and $E(B-V)_{\text{neb}}^{\text{cov}}$. Specifically, dusty galaxies with modest dust-covering fractions and high $E(B-V)_{\text{neb}}^{\text{cov}}$ tend to have higher R_V , while those with higher f_{cov} and modest values of $E(B-V)_{\text{neb}}^{\text{cov}}$ tend to have lower R_V . These results suggest that dusty galaxies may exhibit a range of R_V depending on the actual covering fraction of—and reddening provided by—the dust.

To conclude, the normalization of the nebular attenuation curve shows a positive correlation with the fraction of unobscured light contributing to the observed line fluxes. Galaxies with high R_V values systematically exhibit lower values of f_{cov} and higher $E(B-V)_{\text{neb}}^{\text{cov}}$. Although this analysis specifically addresses the nebular attenuation curve, the general idea that a greater fraction of unobscured sightlines (low f_{cov}) mixed with optically-thick (high $E(B-V)$) sightlines leads to a higher R_V supports the general paradigm outlined for the reddening curves of the *stellar continuum* in young star-forming galaxies, where an increase in unobscured sightlines typically results in flatter (or higher R_V)

attenuation curves (e.g., Witt & Gordon 1996; Calzetti et al. 2000; Narayanan et al. 2018; Trayford et al. 2020). Thus, examining the variation in R_V for nebular attenuation curves can provide insights into the factors that may contribute to variations in R_V for stellar attenuation curves.

Since the AURORA sample is broadly representative of galaxies at $z \sim 1.5 - 4.5$, the average nebular attenuation curve given by Equation 22 should be applicable to statistical samples of star-forming galaxies at these redshifts, and potentially even higher redshifts as well (Section 4.3). However, caution is advised when applying this curve to galaxies whose properties differ significantly from those in the AURORA sample, such as those with $\mathcal{F}_{\text{unred}}$ values near the extremes of the distribution shown in Figure 20. In such cases—i.e., where the covering fraction is high, or where the covering fraction is low and the reddening is high—it may be more appropriate to assume a lower or higher R_V than the one associated with the curve given in Equation 22. The key conclusion of this analysis is that the diversity of shapes and normalizations of the effective nebular attenuation curves presented in Section 4 can be accommodated by assuming the Galactic extinction curve—and therefore similar dust grain properties as seen along Milky Way sightlines—with a sub-unity covering fraction of that dust (Section 5.2).

6. CONCLUSIONS

We used deep JWST/NIRSpec $\lambda = 1 - 5 \mu\text{m}$ spectroscopy from the AURORA survey to measure numerous H I Balmer and Paschen recombination emission lines in 24 individual star-forming galaxies at $z = 1.52 - 4.41$. The measurements were used to derive the nebular attenuation curves and nebular reddening in these galaxies. To interpret the multiple recombination line ratios, we also considered a model that departs from the usual assumption of a uniform screen of dust. The primary results from our analysis are as follows:

- For at least half the galaxies in the sample, the nebular reddening derived from the Paschen lines exceeds the value obtained from the Balmer lines, adopting the usual assumptions of a uniform screen (100% covering fraction) of dust and the Galactic extinction curve (Section 3 and Figure 7). Other standard extinction and attenuation curves in the literature yield similar results. We interpret the systematic offset between the Paschen- and Balmer-inferred reddening as an indication of the presence of star formation that is optically thick in the Balmer lines.
- We used the H I recombination line ratios to calculate the effective nebular attenuation curves of the individual galaxies (Section 4.1). The derived attenuation curves are similar in shape to those of standard extinction and attenuation curves at $\lambda \lesssim 6000 \text{ \AA}$ (Section 4.2). However, at longer wavelengths, the individual nebular attenuation curves for most galaxies diverge from standard extinction and attenuation curves (Figure 8), a behavior that is also reflected in the average nebular dust attenuation curve of the 24 galaxies

(Figure 10). We do not find substantial evidence for any redshift evolution in the shape of the average nebular dust attenuation curve based on the limited data available for $z > 3$ galaxies in the AURORA sample (Section 4.3 and Figure 11).

- The R_V (or normalizations) of the effective nebular attenuation curves are in the range $R_V \simeq 3.2 - 16.4$, considerably higher on average than the values found in a range of environments in the Milky Way (Figure 12), suggesting that the geometry of dust with respect to the stars (i.e., the dust covering fraction, f_{cov}) is driving the variation in R_V (Sections 4.4 and 5.3).
- Based on the offsets between the Balmer and Paschen-inferred reddening and the large R_V values, both of which suggest the importance of the dust-stars geometry on the effective nebular attenuation curves, we explored a model that parameterizes variations in the dust optical depths towards OB associations by assuming a sub-unity covering fraction of dust (Section 5.2). By fitting this model to the observed H I recombination line ratios, we obtained dust covering fractions in the range $f_{\text{cov}} \simeq 0.6 - 1.0$ and line-of-sight reddening values of $E(B - V)_{\text{neb}}^{\text{cov}} \simeq 0.2 - 1.2$ (Figure 16). Thus, our analysis suggests that the diversity of effective nebular attenuation curves can be accounted for by assuming dust grain properties similar to that of Galactic sightlines (i.e., the Galactic extinction curve), but with a subunity covering fraction of dust. The light-weighted reddening at the wavelengths of the Balmer and Paschen lines computed using the covering-fraction model agree well with the corresponding values based purely on the Balmer lines or Paschen lines (Figure 18).
- Further, we find a strong correlation between R_V and the fraction of unreddened light contributing to the observed H I line fluxes (Section 5.5 and Figure 20). Thus, galaxies with unreddened sightlines mixed with optically-thick sightlines have higher R_V values. Dusty galaxies may exhibit a range of R_V depending on the covering fraction of, and reddening provided by, the dust (Figure 21).

The AURORA sample includes typical star-forming galaxies at $z \sim 1 - 4$, with bolometric luminosities and dust obscurations lower than those of the rarer ultraluminous infrared (and brighter) galaxies that are routinely detected individually with ALMA and other far-IR facilities. Yet, even within these typical galaxies of the AURORA sample, we find evidence of optically thick star formation. Though the distribution of dust towards OB associations likely varies on parsec scales, which are too small to resolve for unlensed galaxies even with JWST, our analysis demonstrates that even integrated H I recombination line ratios can provide valuable constraints on the covering fraction of dust and dust-obscured luminosity in these galaxies.

This analysis points to a number of other investigations to further exploit and leverage the exquisite JWST spectroscopy of high-redshift galaxies. While our analysis has focused on the nebular dust attenuation curves of individual galaxies, there are many unexplored avenues that can be pursued by constructing composite spectra in bins of galaxy properties, particularly those which are known to correlate with dust attenuation (e.g., UV slope, stellar mass, gas-phase metallicity, etc.). This will allow us to better understand the factors that modulate the shape and normalization of the nebular dust attenuation curve, including possible variations in the dust grain composition and size distribution. Earlier studies to constrain the shape of the dust attenuation curve of the *stellar continuum* (e.g., Reddy et al. 2015; Shivaeei et al. 2020) can be improved upon with the precise measurements of nebular reddening enabled with JWST/NIRSpec, combined with more extensive and deeper near-IR photometry available with JWST/NIRCam.

Well-constructed composite spectra may yield additional insights into the physical conditions (e.g., level of l -mixing, continuum pumping) modulating the H I recombination line fluxes, in particular by focusing on the higher-order Balmer and Paschen line ratios that are close enough in wavelength that their observed ratios should be similar to the intrinsic ones (e.g., Appendix A). Separately, more precise constraints on R_V can be attained with a similar analysis for galaxies at lower redshifts ($z < 1.67$; Figure 3) where Pa α (Pa4) is accessible within the JWST/NIRSpec wavelength range.

The novel constraints on dust covering fractions towards OB associations may be particularly relevant for understanding several key aspects of high-redshift galaxies. The dust covering fraction likely correlates with gas covering fraction, which in turn has been shown to be a key factor in the escape of ionizing radiation, a topic of importance for studies of reionization (e.g., Zackrisson et al. 2013; Rivera-Thorsen et al. 2015; Trainor et al. 2015; Reddy et al. 2016b; Steidel et al. 2018; Gazagnes et al. 2018; Jaskot et al. 2019; Reddy et al. 2022). Thus, it is important to investigate the connection between dust covering fraction deduced from the H I recombination lines and proxies for H I gas and metal cover-

ing fractions—e.g., from the depths of the Lyman series absorption lines (Reddy et al. 2016b; Steidel et al. 2018; Gazagnes et al. 2018) or the equivalent widths of saturated low-ionization interstellar absorption lines (Shapley et al. 2003; Berry et al. 2012; Jones et al. 2012; Reddy et al. 2016b; Du et al. 2018; Pahl et al. 2020; Reddy et al. 2022). Connecting these covering fractions to properties that may indicate the efficiency of stellar feedback (e.g., wind velocities, SFR surface densities, etc.) will yield valuable insights into the effect of such feedback on the porosity of the ISM and the escape of Ly α and Lyman continuum photons.

The broader implications of the nebular dust attenuation curves presented here, including their impact on dust-corrected line luminosities and line ratios, nebular-based SFRs, and differential reddening of the nebular lines and stellar continuum, are presented in Paper II (Reddy et al., submitted). Additionally, Paper II discusses the calibration between JWST/MIRI dust emission measurements and total SFRs in the context of the H I recombination line analysis. It also presents a joint analysis of the nebular and stellar reddening curves for one of the youngest galaxies in the AURORA sample, GOODS-N-17940.

This work is based on observations made with the NASA/ESA/CSA James Webb Space Telescope. The data were obtained from the Mikulski Archive for Space Telescopes at the Space Telescope Science Institute, which is operated by the Association of Universities for Research in Astronomy, Inc., under NASA contract NAS5-03127 for JWST. The specific observations analyzed can be accessed via doi:10.17909/hvne7139. We also acknowledge support from NASA grant No. JWST-GO-01914. Some of the data products used in this analysis were retrieved from the Dawn JWST Archive (DJA). DJA is an initiative of the Cosmic Dawn Center (DAWN), which is funded by the Danish National Research Foundation under grant DNRF140.

Facility: JWST/NIRSpec

REFERENCES

- Alexandroff, R. M., Heckman, T. M., Borthakur, S., Overzier, R., & Leitherer, C. 2015, *ApJ*, 810, 104
- Baldwin, J. A., Phillips, M. M., & Terlevich, R. 1981, *PASP*, 93, 5
- Battisti, A. J., Calzetti, D., & Chary, R. R. 2017, *ApJ*, 840, 109
- Battisti, A. J., Bagley, M. B., Baronchelli, I., et al. 2022, *MNRAS*, 513, 4431
- Berry, M., Gawiser, E., Guaita, L., et al. 2012, *ApJ*, 749, 4
- Bouwens, R. J., Smit, R., Labbé, I., et al. 2016, *ApJ*, 831, 176
- Bowler, R. A. A., Cullen, F., McLure, R. J., Dunlop, J. S., & Avison, A. 2022, *MNRAS*, 510, 5088
- Buat, V., Boquien, M., Małek, K., et al. 2018, *A&A*, 619, A135
- Burgarella, D., Buat, V., & Iglesias-Páramo, J. 2005, *MNRAS*, 360, 1413
- Calzetti, D. 1997, *AJ*, 113, 162
- Calzetti, D., Armus, L., Bohlin, R. C., et al. 2000, *ApJ*, 533, 682
- Calzetti, D., Kinney, A. L., & Storchi-Bergmann, T. 1994, *ApJ*, 429, 582
- Cardelli, J. A., Clayton, G. C., & Mathis, J. S. 1989, *ApJ*, 345, 245
- Chabrier, G. 2003, *PASP*, 115, 763
- Chartab, N., Newman, A. B., Rudie, G. C., Blanc, G. A., & Kelson, D. D. 2024, *ApJ*, 960, 73
- Clarke, L., Shapley, A. E., Sanders, R. L., et al. 2024, *arXiv e-prints*, arXiv:2406.05178

- Clayton, G. C., Gordon, K. D., & Wolff, M. J. 2000, *ApJS*, 129, 147
- Conroy, C., & Kratter, K. M. 2012, *ApJ*, 755, 123
- Cullen, F., McLure, R. J., Dunlop, J. S., et al. 2019, *MNRAS*, 487, 2038
- Domínguez, A., Siana, B., Henry, A. L., et al. 2013, *ApJ*, 763, 145
- Domínguez-Guzmán, G., Rodríguez, M., García-Rojas, J., Esteban, C., & Toribio San Cipriano, L. 2022, *MNRAS*, 517, 4497
- Draine, B. T. 2003, *ARA&A*, 41, 241
- Du, X., Shapley, A. E., Reddy, N. A., et al. 2018, *ApJ*, 860, 75
- Eisenstein, D. J., Johnson, B. D., Robertson, B., et al. 2023, *arXiv e-prints*, [arXiv:2310.12340](https://arxiv.org/abs/2310.12340)
- Eldridge, J. J., Stanway, E. R., Xiao, L., et al. 2017, *PASA*, 34, e058
- Förster Schreiber, N. M., Roussel, H., Sauvage, M., & Charmandaris, V. 2004, *A&A*, 419, 501
- Ferguson, J. W., & Ferland, G. J. 1997, *ApJ*, 479, 363
- Fetherolf, T., Reddy, N. A., Shapley, A. E., et al. 2021, *MNRAS*, 508, 1431
- Finkelstein, S. L., Bagley, M. B., Ferguson, H. C., et al. 2023, *ApJL*, 946, L13
- Fitzpatrick, E. L. 1999, *PASP*, 111, 63
- Fitzpatrick, E. L., & Massa, D. 2009, *ApJ*, 699, 1209
- Förster Schreiber, N. M., Genzel, R., Lutz, D., Kunze, D., & Sternberg, A. 2001, *ApJ*, 552, 544
- Förster Schreiber, N. M., Genzel, R., Bouché, N., et al. 2009, *ApJ*, 706, 1364
- Fudamoto, Y., Oesch, P. A., Schinnerer, E., et al. 2017, *MNRAS*, 472, 483
- Galliano, F., Galametz, M., & Jones, A. P. 2018, *ARA&A*, 56, 673
- Gazagnes, S., Chisholm, J., Schaerer, D., et al. 2018, *A&A*, 616, A29
- Giménez-Arteaga, C., Brammer, G. B., Marchesini, D., et al. 2022, *ApJS*, 263, 17
- Gordon, K. D., Clayton, G. C., Misselt, K. A., Landolt, A. U., & Wolff, M. J. 2003, *ApJ*, 594, 279
- Harikane, Y., Laporte, N., Ellis, R. S., & Matsuoka, Y. 2020, *ApJ*, 902, 117
- Heckman, T. M., Borthakur, S., Overzier, R., et al. 2011, *ApJ*, 730, 5
- Heintz, K. E., Brammer, G. B., Watson, D., et al. 2025, *A&A*, 693, A60
- Henry, A., Scarlata, C., Martin, C. L., & Erb, D. 2015, *ApJ*, 809, 19
- Hirashita, H. 2012, *MNRAS*, 422, 1263
- Hirashita, H., Nozawa, T., Yan, H., & Kozasa, T. 2010, *MNRAS*, 404, 1437
- Hummer, D. G., & Storey, P. J. 1987, *MNRAS*, 224, 801
- Inami, H., Algera, H. S. B., Schouws, S., et al. 2022, *MNRAS*, 515, 3126
- Isobe, Y., Ouchi, M., Nakajima, K., et al. 2023, *arXiv e-prints*, [arXiv:2301.06811](https://arxiv.org/abs/2301.06811)
- Jaskot, A. E., Dowd, T., Oey, M. S., Scarlata, C., & McKinney, J. 2019, *ApJ*, 885, 96
- Jaskot, A. E., & Ravindranath, S. 2016, *ApJ*, 833, 136
- Jones, T., Stark, D. P., & Ellis, R. S. 2012, *ApJ*, 751, 51
- Jones, T. A., Ellis, R. S., Schenker, M. A., & Stark, D. P. 2013, *ApJ*, 779, 52
- Kashino, D., Silverman, J. D., Rodighiero, G., et al. 2013, *ApJL*, 777, L8
- Kashino, D., Lilly, S. J., Renzini, A., et al. 2022, *ApJ*, 925, 82
- Kennicutt, Jr., R. C., Tamblyn, P., & Congdon, C. E. 1994, *ApJ*, 435, 22
- Kriek, M., Shapley, A. E., Reddy, N. A., et al. 2015, *ApJS*, 218, 15
- Leitherer, C. 1990, *ApJS*, 73, 1
- Li, Q., Narayanan, D., Torrey, P., Davé, R., & Vogelsberger, M. 2021, *MNRAS*, 507, 548
- Lorenz, B., Kriek, M., Shapley, A. E., et al. 2023, *ApJ*, 951, 29
- . 2024, *ApJ*, 975, 187
- Lorenz, B., Suess, K. A., Kriek, M., et al. 2025, *arXiv e-prints*, [arXiv:2505.10632](https://arxiv.org/abs/2505.10632)
- Luridiana, V., Morisset, C., & Shaw, R. A. 2015, *A&A*, 573, A42
- Mesa-Delgado, A., Esteban, C., García-Rojas, J., et al. 2009, *MNRAS*, 395, 855
- Meurer, G. R., Heckman, T. M., & Calzetti, D. 1999, *ApJ*, 521, 64
- Narayanan, D., Conroy, C., Davé, R., Johnson, B. D., & Popping, G. 2018, *ApJ*, 869, 70
- Pahl, A. J., Shapley, A., Faisst, A. L., et al. 2020, *MNRAS*, 493, 3194
- Pengelly, R. M., & Seaton, M. J. 1964, *MNRAS*, 127, 165
- Pentericci, L., Carniani, S., Castellano, M., et al. 2016, *ApJL*, 829, L11
- Pettini, M., Steidel, C. C., Adelberger, K. L., Dickinson, M., & Giavalisco, M. 2000, *ApJ*, 528, 96
- Prescott, M. K. M., Finlator, K. M., Cleri, N. J., Trump, J. R., & Papovich, C. 2022, *ApJ*, 928, 71
- Price, S. H., Kriek, M., Brammer, G. B., et al. 2014, *ApJ*, 788, 86
- Reddy, N. A., Steidel, C. C., Fadda, D., et al. 2006, *ApJ*, 644, 792
- Reddy, N. A., Steidel, C. C., Pettini, M., & Bogosavljević, M. 2016a, *ApJ*, 828, 107
- Reddy, N. A., Steidel, C. C., Pettini, M., Bogosavljević, M., & Shapley, A. E. 2016b, *ApJ*, 828, 108
- Reddy, N. A., Topping, M. W., Sanders, R. L., Shapley, A. E., & Brammer, G. 2023a, *ApJ*, 952, 167
- . 2023b, *arXiv e-prints*, [arXiv:2301.07249](https://arxiv.org/abs/2301.07249)
- Reddy, N. A., Kriek, M., Shapley, A. E., et al. 2015, *ApJ*, 806, 259
- Reddy, N. A., Oesch, P. A., Bouwens, R. J., et al. 2018a, *ApJ*, 853, 56
- Reddy, N. A., Shapley, A. E., Sanders, R. L., et al. 2018b, *ApJ*, 869, 92

- Reddy, N. A., Shapley, A. E., Kriek, M., et al. 2020, *ApJ*, 902, 123
- Reddy, N. A., Topping, M. W., Shapley, A. E., et al. 2022, *ApJ*, 926, 31
- Reddy, N. A., Sanders, R. L., Shapley, A. E., et al. 2023c, *arXiv e-prints*, [arXiv:2302.10213](#)
- Rezaee, S., Reddy, N., Shivaiei, I., et al. 2021, *MNRAS*, 506, 3588
- Rivera-Thorsen, T. E., Hayes, M., Östlin, G., et al. 2015, *ApJ*, 805, 14
- Salim, S., & Boquien, M. 2019, *ApJ*, 872, 23
- Salim, S., & Narayanan, D. 2020, *ARA&A*, 58, 529
- Sanders, R. L., Shapley, A. E., Kriek, M., et al. 2016, *ApJ*, 816, 23
- Sanders, R. L., Shapley, A. E., Topping, M. W., et al. 2024, *arXiv e-prints*, [arXiv:2408.05273](#)
- Sandles, L., D'Eugenio, F., Maiolino, R., et al. 2023, *arXiv e-prints*, [arXiv:2306.03931](#)
- Schouws, S., Stefanon, M., Bouwens, R., et al. 2022, *ApJ*, 928, 31
- Shapley, A. E., Sanders, R. L., Reddy, N. A., Topping, M. W., & Brammer, G. B. 2023, *arXiv e-prints*, [arXiv:2301.03241](#)
- Shapley, A. E., Steidel, C. C., Pettini, M., & Adelberger, K. L. 2003, *ApJ*, 588, 65
- Shapley, A. E., Sanders, R. L., Topping, M. W., et al. 2025, *ApJ*, 980, 242
- Shivaiei, I., Darvish, B., Sattari, Z., et al. 2020, *ApJL*, 903, L28
- Shivaiei, I., Reddy, N. A., Shapley, A. E., et al. 2015, *ApJ*, 815, 98
- Skelton, R. E., Whitaker, K. E., Momcheva, I. G., et al. 2014, *ApJS*, 214, 24
- Stanway, E. R., & Eldridge, J. J. 2018, *MNRAS*, 479, 75
- Steidel, C. C., Bogosavljević, M., Shapley, A. E., et al. 2018, *ApJ*, 869, 123
- Steidel, C. C., Strom, A. L., Pettini, M., et al. 2016, *ApJ*, 826, 159
- Steidel, C. C., Rudie, G. C., Strom, A. L., et al. 2014, *ApJ*, 795, 165
- Storey, P. J., & Hummer, D. G. 1995, *MNRAS*, 272, 41
- Strom, A. L., Steidel, C. C., Rudie, G. C., et al. 2017, *ApJ*, 836, 164
- Theios, R. L., Steidel, C. C., Strom, A. L., et al. 2019, *ApJ*, 871, 128
- Topping, M. W., Shapley, A. E., Reddy, N. A., et al. 2020, *MNRAS*, 495, 4430
- Topping, M. W., Sanders, R. L., Shapley, A. E., et al. 2025, *arXiv e-prints*, [arXiv:2502.08712](#)
- Trainor, R. F., Steidel, C. C., Strom, A. L., & Rudie, G. C. 2015, *ApJ*, 809, 89
- Trainor, R. F., Strom, A. L., Steidel, C. C., et al. 2019, *ApJ*, 887, 85
- Trayford, J. W., Lagos, C. d. P., Robotham, A. S. G., & Obreschkow, D. 2020, *MNRAS*, 491, 3937
- Valentino, F., Brammer, G., Gould, K. M. L., et al. 2023, *ApJ*, 947, 20
- van der Wel, A., Chang, Y.-Y., Bell, E. F., et al. 2014, *ApJL*, 792, L6
- Vasei, K., Siana, B., Shapley, A. E., et al. 2016, *ApJ*, 831, 38
- Willott, C. J., Carilli, C. L., Wagg, J., & Wang, R. 2015, *ApJ*, 807, 180
- Witt, A. N., & Gordon, K. D. 1996, *ApJ*, 463, 681
- Zackrisson, E., Inoue, A. K., & Jensen, H. 2013, *ApJ*, 777, 39
- Zhang, R., Yuan, H., & Chen, B. 2023, *ApJS*, 269, 6

APPENDIX

A. VARIATIONS IN THE INTRINSIC LINE RATIOS WITH ELECTRON TEMPERATURE AND ASSUMED LEVEL OF L -MIXING

The default values of the intrinsic line ratios adopted in this analysis were obtained from PyNeb, assuming $n_e = 100 \text{ cm}^{-3}$ and $T = 15,000 \text{ K}$ (Table 1). In the following, we explore how different assumptions of the H II region temperature and level of l -mixing affect these line ratios, and the impact on several of the most important quantities discussed in this analysis. To aid the following discussion, it is useful to define the parameter, f_{lr} , as the fractional variation in an intrinsic line ratio relative to the default value listed in Table 1:

$$f_{lr} = \left(\frac{f_0(\lambda)}{f_0(\text{H}\alpha)} \right) / \left(\frac{f_0(\lambda)}{f_0(\text{H}\alpha)} \right)_{\text{def}}, \quad (\text{A1})$$

where the denominator is the default intrinsic line ratio.

The top panel of Figure 22 shows f_{lr} for three combinations of n_e and T , based on the values reported by PyNeb. For the range of n_e inferred for high-redshift star-forming galaxies ($n_e \lesssim 1000 \text{ cm}^{-3}$), there is little variation in the intrinsic line ratios at a fixed T . For the Paschen lines, density effects become important at $n_e \gtrsim 10^5 \text{ cm}^{-3}$, which causes these lines to be weaker relative to the Balmer lines (Ferguson & Ferland 1997). For the Balmer lines, density effects only become important closer to the critical density of $\simeq 10^8 \text{ cm}^{-3}$. In contrast, variations in the electron temperature within the range found for H II regions can cause non-negligible shifts in the higher-order Balmer and Paschen lines. For example, for high-metallicity galaxies with $T \approx 7,000 \text{ K}$, the H12-to-H α ratio is $\approx 0.92\%$ of the default value. Qualitatively, higher temperatures (corresponding to lower metallicity H II regions) lead to a larger fraction of electrons occupying higher- n states, resulting in an increased emissivity of the high-order lines relative to the low-order lines of the same series.

The H I line emissivities reported by PyNeb are taken from Hummer & Storey (1987) and Storey & Hummer (1995), who present the most definitive calculations of these emissivities for a 1000-level H atom, considering all angular momentum (l) states. Pengelly & Seaton (1964) calculate, as a function of density, the n level above which the collisional rate exceeds the radiative lifetime, such that perturbations from collisions cause electrons to mix between different angular momentum states, a process known as l -mixing. This in turn alters the transition probabilities and resulting line emissivities. For instance, these authors calculate that all levels with $n \gtrsim 25$ are well mixed for $n_e \sim 100 \text{ cm}^{-3}$.

The bottom panel of Figure 22 shows f_{lr} for intrinsic line ratios computed from Cloudy v23.01 by invoking an H atom with 25 l -resolved levels and an additional 300 “collapsed” levels that are well mixed, or thermalized (the “Cloudy-n25” model). In the bottom panel, the default line ratios used to

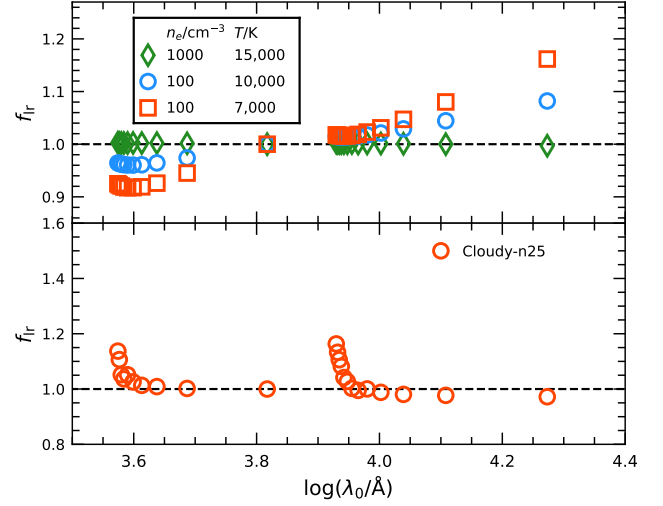


Figure 22. Fractional variation in the intrinsic line ratios relative to the default values reported by PyNeb and listed in Table 1, which assume $n_e = 100 \text{ cm}^{-3}$ and $T = 15,000 \text{ K}$. The top panel shows the effect of increasing the electron density by an order of magnitude ($n_e = 1000 \text{ cm}^{-3}$ at the same temperature as the default model (green diamonds). Also shown are two other models with $n_e = 100 \text{ cm}^{-3}$ and lower temperatures of $T = 10,000 \text{ K}$ and $7,000 \text{ K}$ (blue circles and red squares, respectively). The bottom panel shows the fractional variation in the intrinsic line ratios for different assumptions of l -mixing, computed using Cloudy modeling (see text).

define f_{lr} are taken from PyNeb for $T = 10,000 \text{ K}$ —which is close to the average value computed by Cloudy over all ionization zones of the H II region—and $n_e = 100 \text{ cm}^{-3}$. As expected, the largest discrepancies in the line ratios occur for the highest-order Balmer and Paschen lines, as these high n -levels are more significantly affected by the degree of l -mixing.

It is useful to examine whether the observed line ratios obtained with AURORA are consistent with the predicted intrinsic line ratios. Specifically, H12 and H9 are far enough apart in wavelength that their ratio can provide some leverage on the models shown in Figure 22, yet they are still close enough in wavelength that their observed line ratio should be close to the intrinsic value. A comparable analysis can be applied to the high-order Paschen lines (e.g., Pa14 and higher), although these lines are relatively weaker and thus provide less constraining power.

Figure 23 displays the H9 and H12 fluxes of the 22 galaxies in the AURORA parent sample that have $> 5\sigma$ detections of both lines. The intrinsic ratio of H9-to-H12 is indicated by the dashed and solid lines for the default PyNeb values adopted in this analysis and for the Cloudy model discussed above, respectively. Interestingly, the observed H9/H12 ra-

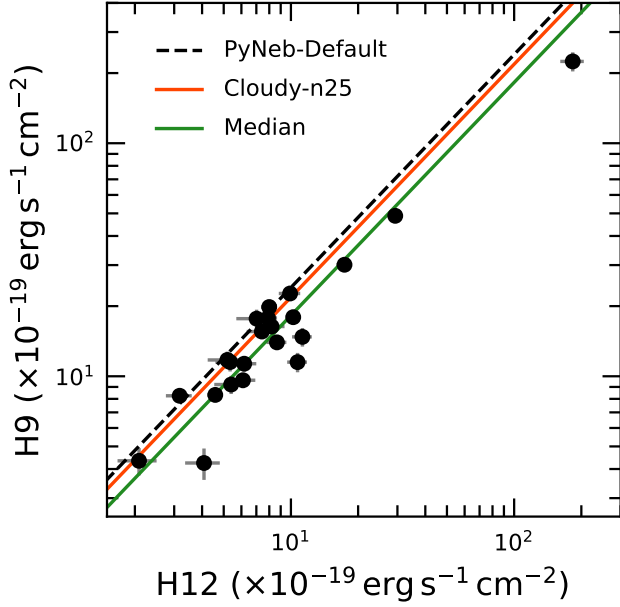


Figure 23. Comparison of the H9 and H12 fluxes of 22 galaxies in the parent AURORA sample with $> 5\sigma$ detections of both lines. The dashed line indicates the expected intrinsic ratio of H9/H12 as reported by PyNeb using the default values of $n_e = 100 \text{ cm}^{-3}$ and $T = 15,000 \text{ K}$. The intrinsic ratios calculated with the Cloudy-n25 model described in the text is shown by the red line. The green line denotes the observed median ratio of H9/H12.

tios for the majority of galaxies are systematically and significantly lower than the intrinsic values reported by PyNeb and Cloudy-n25 (varying the temperature does little to alter the intrinsic ratio), in the opposite direction one would expect if the ratio is modified by dust reddening. The observed median ratio of H9/H12 is indicated by the green line. A similar conclusion is reached if only the 6 objects with $> 10\sigma$ detections of both lines are considered: these objects have the highest equivalent widths, W_λ , of the Balmer lines where systematic uncertainties in the stellar Balmer absorption corrections are minimal, and where possible variations in the continuum fit under the lines should not materially affect the line ratios. The offsets between the observed and intrinsic ratios may indicate Case A conditions—which result in a lower intrinsic H9/H12 ratio than the Case B prediction—or possibly different degrees of l -mixing or continuum-pumping of the H I lines through stellar absorption (e.g., see Mesa-Delgado et al. 2009; Domínguez-Guzmán et al. 2022 for similar observations in the Orion Nebula and H II regions in the Magellanic Clouds, respectively).

Whatever processes may be at play in modulating the H12 and H9 line emissivities it is useful to examine how altering the intrinsic ratios affects several of the key quantities discussed in this analysis, including f_{cov} , $E(B - V)_{\text{neb}}^{\text{cov}}$, $E(B - V)_{\text{neb}}^{\text{eff}}$, R_V , $A_{\text{neb}}^{\text{eff}}$, and SFR_{neb} . Figure 24 shows the comparison of the values derived with the default PyNeb assumption ($T = 15,000 \text{ K}$) and those obtained with the

Cloudy-n25 intrinsic ratios (red circles). Additionally, the green circles denote the values obtained if we fix the intrinsic ratios of H9/H10, H10/H11, and H11/H12 to the median observed values. Though there are a few outliers for some of the parameters (e.g., f_{cov} and $E(B - V)_{\text{neb}}^{\text{cov}}$), for the vast majority of galaxies in the sample, there are no large systematic offsets larger than the measurement uncertainties. For the most part, there is a one-to-one correspondence in the variables derived using different sets of intrinsic line ratios, such that the ordering of objects in parameter space is preserved (e.g., those with high f_{cov} using the default intrinsic line ratios have similarly high f_{cov} using the modified intrinsic line ratios). Thus, all of the correlations discussed in the analysis are preserved regardless of which sets of intrinsic line ratios are assumed.

B. TESTING FOR BIASES IN THE COVERING-FRACTION MODEL

Figure 16 shows that, on average, the uncertainties in both $E(B - V)_{\text{neb}}^{\text{cov}}$ and f_{cov} increase with f_{cov} . Here, we examine whether these larger uncertainties are driven by a limited baseline in wavelength of the fitted lines, a lower number of fitted lines, and/or a lower S/N in the lines. Figure 25 shows the uncertainties in f_{cov} and $E(B - V)_{\text{neb}}^{\text{cov}}$ plotted against the wavelength distribution, number, and S/N of the Balmer and Paschen recombination emission lines for each of the 24 galaxies in the sample. From the top left panel of the figure, it is apparent that the wavelength coverage of the Balmer and Paschen lines used to fit R versus λ_0 for the one galaxy with the largest $\sigma(f_{\text{cov}})$ is similar to the wavelength coverage accessible for galaxies with the lowest $\sigma(f_{\text{cov}})$. However, this galaxy has a lower wavelength density of both higher-order Balmer and higher-order Paschen lines relative to other galaxies in the sample. Thus, while the total number of lines does not appear to be a strong factor in predicting $\sigma(f_{\text{cov}})$ (top middle panel), the wavelength density of lines does appear to play a role. The top right panel clearly indicates that the galaxy with the largest $\sigma(f_{\text{cov}})$ has fewer higher S/N lines relative to galaxies with lower $\sigma(f_{\text{cov}})$. This galaxy is sufficiently faint that there are fewer high S/N lines, and hence fewer of the weaker higher-order Balmer and Paschen lines with $S/N > 5$, available for our analysis. The same general conclusions hold for galaxies with higher $\sigma(E(B - V)_{\text{neb}}^{\text{cov}})$ (bottom row of Figure 25).

We next consider whether the covering-fraction modeling is biased towards lower f_{cov} for galaxies with lower S/N lines and a sparser wavelength coverage of those lines. To test for such an effect, the S/N of all the lines for every galaxy in the sample was degraded by simply multiplying the flux uncertainties by a factor of 3. This typically resulted in anywhere from 12% to 50% of the lines for any given galaxy falling below $S/N = 5$. These lines were removed

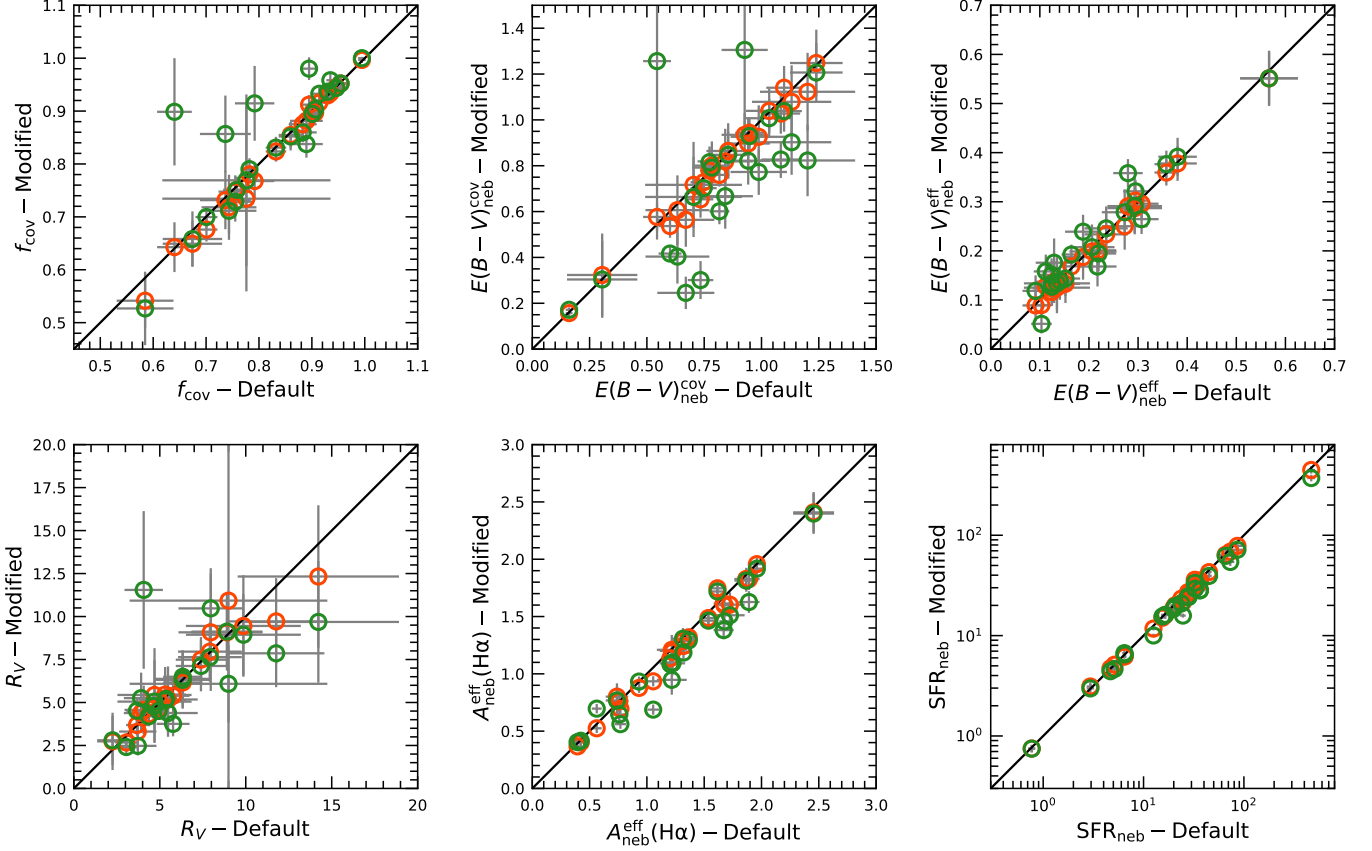


Figure 24. Effect of adjusting the intrinsic H I recombination line ratios on several quantities analyzed in this work, including f_{cov} , $E(B - V)_{\text{neb}}^{\text{cov}}$, $E(B - V)_{\text{neb}}^{\text{eff}}$, R_V , $A_{\text{neb}}^{\text{eff}}(\text{H}\alpha)$, and SFR_{neb} . In each panel, the open red and blue circles indicate values obtained with the intrinsic ratios from the Cloudy-default and PyNeb $T = 10,000$ K models (see text).

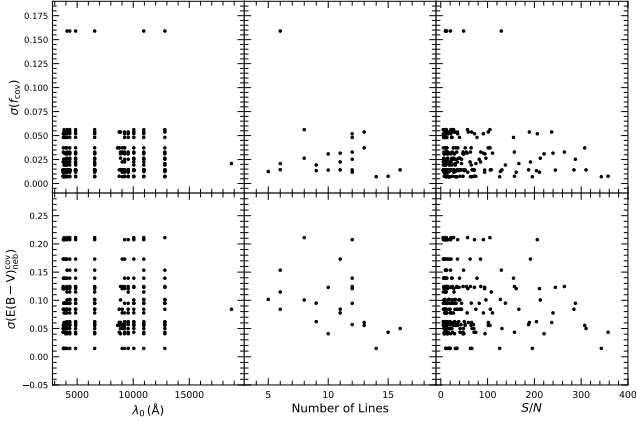


Figure 25. Uncertainties in f_{cov} (top row) and $E(B - V)_{\text{neb}}^{\text{cov}}$ (bottom row) versus line wavelength (left column), number of lines (middle column), and line S/N (right column) for the 24 galaxies in the sample.

(leaving anywhere between 5 and 13 lines⁴), and the fluxes and flux uncertainties of the remaining lines with $S/N \geq 5$ were used to calculate R and σ_R and then re-determine f_{cov} and $E(B - V)_{\text{neb}}^{\text{cov}}$ and their respective uncertainties. Figure 26 compares f_{cov} and $E(B - V)_{\text{neb}}^{\text{cov}}$ obtained with the original data to the values obtained with the degraded- S/N lines. The effect of degrading the lines and removing any with $S/N < 5$ does not introduce a significant systematic offset compared to the measurement uncertainties for either f_{cov} or $E(B - V)_{\text{neb}}^{\text{cov}}$. If anything, there is a slight tendency for the covering-fraction model to settle on slightly *higher* f_{cov} relative to the input value when degrading the S/N (and number) of lines. Thus, the results of this test suggest that any bias towards finding a lower f_{cov} for galaxies with lower S/N and/or fewer lines is not significant, particularly when compared with the measurement uncertainties. In other words, higher S/N spectra of those galaxies with larger uncertainties in f_{cov} and $E(B - V)_{\text{neb}}^{\text{cov}}$ is unlikely to substantially shift the best-fit f_{cov} and $E(B - V)_{\text{neb}}^{\text{cov}}$ to higher and

⁴ Three galaxies had only 2 to 4 lines remaining after this procedure, falling below the minimum of 5 lines required for our analysis, and so were removed from this test.

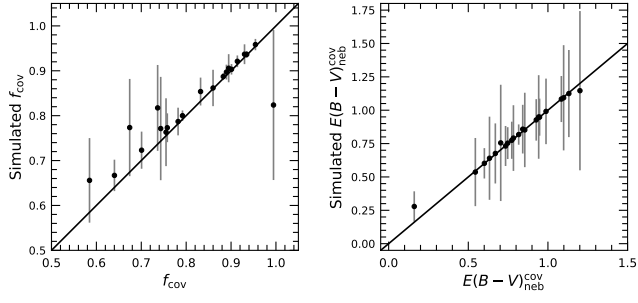


Figure 26. Comparison between f_{cov} and $E(B - V)_{\text{neb}}^{\text{cov}}$ deduced from the measured lines and those obtained when degrading the S/N of all lines by a factor of 3 and removing any lines with $S/N < 5$.

lower values, respectively. As discussed in Paper II, galaxies with lower f_{cov} are associated with lower-SFR galaxies.